Theoretical Study of Topics in the Interaction of Laser and Under-dense Plasma:
THz Radiation by Counter Pulses,
Plasma Diagnostics by Raman Scattering
and Electron Injection in Laser Wakefield Acceleration

Myung-Hoon Jo(Cho)

Department of Physics

Graduate school of UNIST

ULSAN NATIONAL INSTITUTE OF
SCIENCE AND TECHNOLOGY

Theoretical Study of Topics in the Interaction of Laser and Under-dense Plasma: THz Radiation by Counter Pulses, Plasma Diagnostics by Raman Scattering and Electron Injection in Laser Wakefield Acceleration

A dissertation submitted to
the Graduate School of UNIST
in partial fulfillment of the
requirements for the degree of Doctor Philosophy of Science

Myung-Hoon Jo(Cho)

12. 17. 2014
Approved by

Minsup Hur

Advisor

Min Sup Hur

Theoretical Study of Topics in the Interaction of Laser and Under-dense Plasma: THz Radiation by Counter Pulses, Plasma Diagnostics by Raman Scattering and Electron Injection in Laser Wakefield Acceleration

Myung-Hoon Jo(Cho)

This certifies that the dissertation of Myung-Hoon Jo(Cho) is approved.

12. 17. 2014

Advisor:	**Min Sup Hur**
Committee Member:	**Eunmi Choi**
Committee Member:	**Moses Chung**
Committee Member:	**Min-Suk Kwon**
Committee Member:	**Hyyong Suk**

Abstract

Theoretical Study of Topics in the Interaction of Laser and Underdense Plasma: THz Radiation by Counter Pulses, Plasma Diagnostics by Raman Scattering, and Electron Injection in Laser Wakefield Acceleration

Myung Hoon Jo(Cho)

Department of Physics in UNIST

Laser-plasma interaction is an interesting field with numerous practical and scientific applications. In this thesis, I will present three topics in the system of laser and underdense plasma: terahertz (THz) generation by a current driving near cutoff of plasma, plasma diagnostics by Raman scattering, and particle injection in laser wake field acceleration. For the first issue, I will present a new mechanism of generating THz using colliding laser pulses in a magnetized plasma. In this scheme, a THz radiation with a monochromatic feature and high power of 0.1MW was observed. Every aspect of the phenomena was analyzed successfully by a new theory. From this study, I and my collaborators found a new physics of growing electromagnetic field in the range of cut-off frequency. As a 2nd topic, a new diagnosing method of magnetized plasmas is presented. A simple theory of X-mode dispersion relation indicates that frequency shift of Raman backward scattering is much sensitive to the magnetic field than the Raman forward scattering. It is shown that such a difference between RBS and RFS can be used for measuring the magnetic field and plasma density simultaneously. The result is compared with 1D PIC simulation. In the final topic, I will discuss an improved theoretical condition of electron trapping into the ellipsoidal bubble in laser wake field acceleration. The improved theory describes better the electron injection in a more generally shaped bubble than just the previous spherical bubble model, and also exhibits good agreement with the 3D PIC simulations. In addition these topics require different PIC techniques. I will also briefly introduce various numerical techniques used in simulating those topics.

Contents

III. Terahertz radiation by colliding lasers in magnetized plasmas

IV. Measuring the magnetic field of a magnetized plasma using Raman scattering

V. Electron trapping by a transversely ellipsoidal bubble in the laser wake-field acceleration

List of Figures

List of Table

Chapter 1

Introduction

Light-matter interaction is one of the most critical topics in physics. In particular, laser-plasma interaction is definitely an important field because of various and vast applications such as energy fusion, particle acceleration, plasma diagnosis, radiation sources, and so on. In the area of particle acceleration, electron and ion acceleration are hot issues. Laser driven and particle driven wake field accelerations (LWFA and PWFA) are representatives of electron acceleration. Though many studies show the great efficiency of high electron energy, the charge of electrons ($\sim pC$) and shot to shot stability are not good for real applications. So it still needs more studies. Ion acceleration is done by irradiating a high power laser at various targets like gas and thin film. Many researchers are trying to enhance ion energy, but it still limited to under $100\mathrm{MeV}$. As a radiation source, X-rays and Terahertz generation are widely studied. X-rays can be generated by betatron oscillation of trapped electrons in the plasma wake bubble or can be generated by the Compton scattering from a laser and accelerated electrons. Terahertz radiation (1-10THz) is also possible by controlling plasma's density, since it relates to the plasma oscillation. In Tokamak, plasma diagnostics are important for controlling plasmas. Confinement of magnetized plasmas is an especially hot issue, so measuring plasma is prerequisite to study plasma instability. Applications have become realistic with development of laser technology and moreover the laser intensity has been increased enormously, as high as $10^{22}W/cm^2$. This thesis will cover three topics of laser-plasma interaction: Terahertz generation, plasma diagnostics, and LWFA. These topics have many differences such as analysis methods, theory, laser features and condition of plasmas.

Basically, theories of laser-plasma interaction consider the factors of applied external field, temperature, particles' collision, ions' and electrons' motion, and so on. If the laser is strong enough compared to the external field or temperature and at the same time not interacting with enough ions, the situation becomes much simpler. The plasma can be treated as 'cold' plasma composed of electrons only. Even though the conditions are well confined, theoretical calculations are often complicated and moreover many phenomena need non-linear analyses. In addition to the complexity of analysis, because laser-plasma interaction lasts a very short time ranging from the order of femto second (fs) to pico second (ps), computer simulation has become an important tool for research.

This thesis is organized as follows. Chapter 2 describes various PIC techniques. As the first topic, Terahertz radiation by colliding lasers in magnetized plasmas is introduced in Chapter 3. Chapter 4 is about plasma diagnosis using Raman scattering, and LWFA is in Chapter 5. Before discussing these topics, in this Chapter, I will introduce some basic theories.

1.1 Maxwell equation

To describe laser-plasma interaction, various forms of Maxwell equations are customarily employed. The basic form of Maxwell's equations is:

$$\nabla \cdot \mathrm{E} = \mathrm{e}\frac{n_i - n_e}{\varepsilon_0}, \tag{1.1}$$

$$\nabla \times \mathrm{E} + \frac{\partial \mathrm{B}}{\partial \mathrm{t}} = 0, \tag{1.2}$$

$$\nabla \times \mathrm{B} - \frac{1}{c^2}\frac{\partial \mathrm{E}}{\partial \mathrm{t}} = -\frac{\mathrm{e}}{\varepsilon_0 c^2}(n_e v_e + n_i v_i) \tag{1.3}$$

, where e, n_i, n_e, v_e, v_i, and ε_0 are electron charge, ion density, electron density, electron velocity, ion velocity, and vacuum permittivity, respectively. If the electric field is not strong enough to affect ion motion, the ion velocity becomes $v_i \sim 0$ and the ion density is assumed to be the background density $(n_i = n_0)$.

Defining electric and magnetic fields E and B as the vector and scalar potentials A and φ, respectively, the scalar-vector-potential form of Maxwell's equation follows :

$$\mathrm{B} = \nabla \times \mathrm{A}, \tag{1.4}$$

$$\mathrm{E} = -\nabla\varphi - \frac{\partial \mathrm{A}}{\partial \mathrm{t}}. \tag{1.5}$$

Using Eq. (1.4) and (1.5), Eq. (1.1) and (1.3) are rewritten as :

$$\nabla^2(A_x - \varphi) = 1 - \mathrm{n}\left(1 - \frac{p_x}{\gamma}\right) + \left(\frac{\partial}{\partial t} + \frac{\partial}{\partial x}\right)(\nabla \cdot A) + \frac{1}{2}\frac{\partial}{\partial \mathrm{t}}\left(\frac{\partial}{\partial t} - \frac{\partial}{\partial x}\right)(A_x - \varphi), \tag{1.6}$$

$$\nabla \times \nabla \times A + \mathrm{n}\frac{p}{\gamma} + \frac{\partial}{\partial \mathrm{t}}\left(\frac{\partial A}{\partial t} + \frac{\partial \varphi}{\partial x}\right) = 0 \tag{1.7}$$

, where p and γ are the momentum and the relativistic gamma factor of electron, respectively. All units are dimensionless by normalizing the time to $1/\omega_p$, the lengths to c/ω_p, the velocity to c, the vector potential to mc/e, the scalar potential to mc^2/e, the momentum to mc and the density to n_0.

These different forms of Maxwell's equations are used for different analyses. The basic form (Eq. (1.1)-(1.3)) is useful for the Terahertz generation in Chapter 3 and plasma diagnostics in Chapter 4, while the potential form (Eq. (1.6) and (1.7)) is for the LWFA in Chapter 5.

1.2 Bubble formation of the laser wake field

When a high power laser pulse propagates in plasmas, the laser pulse pushes electrons away and as the laser pulse passes through plasmas, expelled electrons try to get back to the original position because of the electric field induced by the charge separation. This process makes a wake field or a “bubble” when the laser pulse is strong enough (See Chapter 5 Fig. 5.5). This wake field is a kind of static electric field and it has a very high electric field amplitude in the range of $10-100\mathrm{GV/m}$. An LWFA uses this strong electric field to accelerate electrons. For comparison, a conventional Radio Frequency(RF) cavity has the range of $10-100\mathrm{MV/m}$ (Fig. 1-1). So an LWFA has more than 1000 times the efficiency of the RF cavity. To use a wake field to accelerate electrons, the process of electron injection into the wake bubble is necessary. Therefore it is important to make bubble formation and understand the mechanism of electron injection.

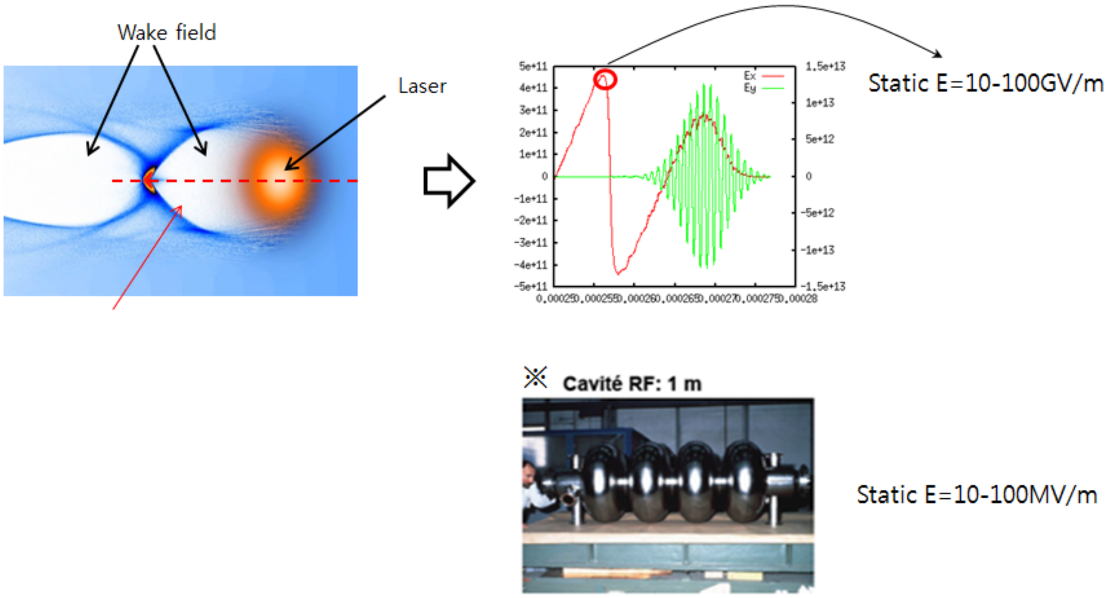

Figure 1.1 : When a high power laser propagates in plasmas, a wake field is generated behind the laser. This wake field is a kind of electro static field and has a very strong electric field amplitude.

If we assume the quantities x and t depend on $\xi = x - v_0 t$, Eq. (1.6) and (1.7) are reduced to the form :

$$\nabla^2 \Phi = \frac{3}{2}(1-n) + \frac{1}{2} n \frac{p_x}{\gamma} - \frac{1}{2}\frac{\partial}{\partial \xi}(\nabla_\perp \cdot \mathrm{A}_\perp), \tag{1.8}$$

$$\nabla_\perp{}^2 \mathrm{A}_\perp - \nabla_\perp(\nabla_\perp \cdot \mathrm{A}_\perp) = \mathrm{n}\frac{p_\perp}{\gamma} + \frac{1}{2}\nabla_\perp \frac{\partial \Phi}{\partial \xi} \tag{1.9}$$

, where $\Phi \equiv A_x - \varphi$ is defined as the wake potential, and the terms which are proportional to ${\gamma_0}^{-2} \ll 1$ are neglected.

Inside the bubble with the assumption of $n = 0$ and $\mathrm{A}_\perp = 0$, the solution of Eq. (1.8) is

$$\Phi = 1 - \frac{R^2}{4} + \frac{r^2}{4}, \qquad A_x = -\varphi = \frac{\Phi}{2}. \tag{1.10}$$

As indicated in Eq. (1.10), the wake potential has a sphere shape which is ‘the spherical bubble model’[3]. Moreover, the wake field is composed of an electric field and a magnetic field.

When $n \neq 0$ and $\mathrm{A}_\perp = 0$, Eq. (1.6) reduces to the form

$$\begin{aligned} \partial_\perp{}^2 \Phi &= 1 - n + n\frac{p_x}{\gamma} = 1 - n + n v_x \\ \partial_y{}^2 \Phi = \partial_y{}^2 \Phi &= \frac{1}{2}(1 - n + n v_x) = \frac{1}{2} n_2 \end{aligned} \tag{1.11}$$

and the remain term $\partial_\xi{}^2 \Phi$ is obtained by inserting Eq. (1.11) into Eq. (1.8) :

$$\partial_\xi{}^2 \Phi = \frac{1}{2}(1 - n - n v_x) = \frac{1}{2} n_1. \tag{1.12}$$

So the solution is :

$$\Phi = \Phi_0 + n_1 \frac{\xi^2}{4} + n_2 \frac{y^2}{4} + n_2 \frac{z^2}{4}. \tag{1.13}$$

This has an ellipsoid shape which is ‘the ellipsoidal bubble’ [4].

From the theoretical aspect, the spherical and ellipsoidal bubble have a fast velocity, close to the speed of light, as long as low density plasma is used. Because plasma’s motion is governed by plasma wave length or plasma frequency, a spherical bubble is formed when the laser spot size is comparable to the plasma wave length. Moreover, the ellipsoidal bubble is possible when the laser spot size is bigger than the plasma wave length.

1.3 Electron injection into the spherical bubble

If we assume that a spherical electron cavity is formed behind a laser, it can be modeled as a moving spherical potential with a velocity of v_0. The trapping condition is introduced in Ref. [5]. Here I will show the detailed derivation of the trapping condition.

As shown in Eq. (1.10), the potential and longitudinal vector potential are given

$$A_x = -\varphi = \frac{r^2}{8}. \tag{1.14}$$

Then from the Hamiltonian :

$$H(\vec{r},t) = \sqrt{1 + (\vec{P} + \vec{A})^2} - v_0 P_x - \varphi \tag{1.15}$$

, where *P* is the canonical momentum of electrons. The equations of motion in terms of the canonical momentum are given as follows :

$$\begin{gathered}
\frac{dP_x}{dt} = -v_x \frac{\partial A_x}{\partial \xi} - v_y \frac{\partial A_y}{\partial \xi} + \frac{\partial \varphi}{\partial \xi} = -v_x \frac{\xi}{4} - \frac{\xi}{4}, \\
\frac{dA_x}{dt} = \frac{\partial A_x}{\partial \xi}\frac{d\xi}{dt} + \frac{\partial A_\xi}{\partial y}\frac{dy}{dt} = \frac{\xi}{4}(v_x - v_0) + \frac{y}{4} v_y, \\
\frac{dP_y}{dt} = -v_x \frac{\partial A_x}{\partial y} - v_y \frac{\partial A_y}{\partial y} + \frac{\partial \varphi}{\partial y} = -v_x \frac{y}{4} - \frac{y}{4}.
\end{gathered} \tag{1.16}$$

Using Eq. (1.16), the equations of motion in terms of the kinetic momentum have the forms:

$$\begin{gathered}
\frac{dp_x}{dt} = \frac{dP_x}{dt} + \frac{dA_x}{dt} = -(1 + v_0)\frac{\xi}{4} + \frac{y}{4}\frac{p_y}{\gamma} \\
\frac{dp_y}{dt} = \frac{dP_y}{dt} = -\left(1 + \frac{p_x}{\gamma}\right)\frac{y}{4} \\
\frac{d\xi}{dt} = \frac{p_x}{\gamma} - v_0 = v_x - v_0 \\
\frac{dy}{dt} = \frac{p_y}{\gamma} = v_y
\end{gathered} \tag{1.17}$$

, where *p* is the kinetic momentum. Using $\gamma = \sqrt{1 + {p_x}^2 + {p_y}^2}$ in 2D, we can set up the equation:

$$\frac{d(\gamma - v_0 p_x)}{dp_x} = \frac{\partial(\gamma - v_0 p_x)}{\partial p_x} + \frac{\partial(\gamma - v_0 p_x)}{\partial p_y}\frac{dp_y}{dp_x} = \frac{d\xi}{dt} + \frac{p_y}{\gamma}\frac{dp_y}{dp_x}. \tag{1.18}$$

Then the *x* directional electron motion is given:

$$
\begin{aligned}
d(\gamma - v_0 p_x) &= \frac{dp_x}{dt} d\xi + \frac{p_y}{\gamma} dp_y \\
&= \left\{-(1+v_0)\frac{\xi}{4} + \frac{y}{4}\frac{p_y}{\gamma}\right\} d\xi + \frac{p_y}{\gamma} dp_y \\
&= -(1+v_0)\frac{\xi}{4} d\xi + \frac{y}{4}\frac{p_x}{\gamma} dy - v_0 \frac{y}{4} dy + \frac{p_y}{\gamma} dp_y. \qquad (1.19)
\end{aligned}
$$

Similarly, the y directional electron motion has the form:

$$\frac{d\gamma}{dp_y} = \frac{\partial \gamma}{\partial p_y} + \frac{\partial \gamma}{\partial p_x}\frac{dp_x}{dp_y} = \frac{dy}{dt} + \frac{p_x}{\gamma}\frac{dp_x}{dp_y} \qquad (1.20)$$

$$
\begin{aligned}
d\gamma &= \frac{dp_y}{dt} dy + \frac{p_x}{\gamma} dp_x \\
&= -\frac{y}{4} dy - \frac{y}{4}\frac{p_x}{\gamma} dy + \frac{p_x}{\gamma} dp_x. \qquad (1.21)
\end{aligned}
$$

Then Eq. (1.19) and (1.21) reduce to the form:

$$d(\gamma - v_0 p_x) = -(1+v_0)\frac{\xi}{4} d\xi - (1+v_0)\frac{y}{4} dy \qquad (1.22)$$

, where the relationship is used as follows

$$d\gamma = \frac{p_y}{\gamma} dp_y + \frac{p_x}{\gamma} dp_x. \qquad (1.23)$$

The solution of Eq. (1.22) is given

$$\gamma - v_0 p_x - 1 = -(1+v_0)\left(\frac{\xi^2}{8} + \frac{y^2}{8} - \frac{R^2}{8}\right) \approx -2\left(\frac{r^2}{8} - \frac{R^2}{8}\right). \qquad (1.24)$$

This gives the information of an electron’s position and momentum in the spherical bubble potential. The trajectory of trapped electrons goes from the top of the bubble with zero velocity to the tail of the bubble with high velocity. At the moment of trapping, electrons may have zero momentum in the y direction, $p_y = 0$ as shown in Fig. 1.2. Then the initial conditions are

$$
\begin{gathered}
y(t=0) = R \\
p_x(t=0) = p_y(t=0) = p_y(t=T) = 0 \qquad (1.25) \\
\gamma(t=T) = \sqrt{1 + {p_x}^2}
\end{gathered}
$$

, where T is the time when electrons start to be trapped at the tail of the bubble.

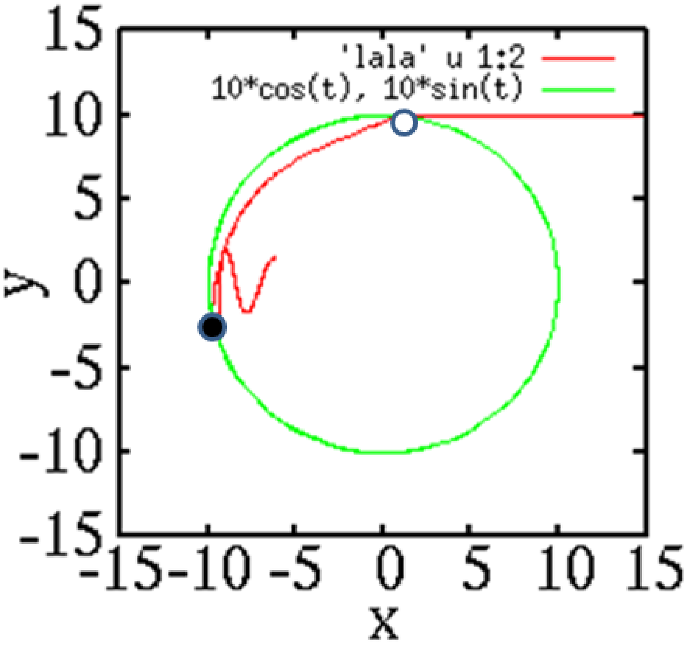

Figure 1.2 : The trapping trajectory of an electron in a spherical potential.
The electron starts to interact with the potential at the top of the bubble (white dot)
and starts to be trapped at the tail of the bubble (black dot).

Because $p_x(T) \gg 1$, γ and v_0 can use the approximated form

$$\begin{aligned} \gamma(T) &\approx p_x + \frac{1}{2p_x} \\ v_0 &\approx 1 - \frac{1}{2{\gamma_0}^2}. \end{aligned} \tag{1.26}$$

The electron trapping may occur when $r < R$, so using Eq. (1.26), Eq. (1.24) gives the trapping condition as follows

$$\frac{p_x(T)}{2{\gamma_0}^2} + \frac{1}{2p_x(T)} > 1 \tag{1.27}$$

The rest of the process is well described in Ref. [5] and the relation is $p_x(T) \sim R^2$. The resultant trapping condition is

$$\gamma_0 < \frac{R}{\sqrt{2}}. \tag{1.28}$$

As shown in Fig. 1.2, the initially motionless electron is accelerated by the bubble potential while moving around the back of the bubble. When the relativistic gamma factor of the bubble is lower than $R/\sqrt{2}$, the electrons catch up to the bubble's velocity (v_0). In other words, the electrons are become trapped.

This theory is about a stationary potential, but in real situations the bubble shape changes and the bubble size also expands or shrinks with time. The injection theory with bubble expansion is introduced in Ref. [6] as a non-stationary potential. In this thesis, I will use a stationary bubble potential, especially I will cover an ellipsoidal potential case in Chapter 5.

1.4 Raman scattering

Various instabilities of plasmas can be occurred by irradiating lasers into plasmas. When the laser pulse length is effectively larger than plasma wavelength, the laser light scatters plus an electron plasma wave (the Raman instability) or an ion acoustic wave (the Brillouin instability). Now let's assume the laser intensity is not high enough to interact with ions, so let Brillouin scattering be neglected. Raman scattering can be explained by using simple frequency and wave number matching condition which comes from momentum conservation

$$\begin{gathered}\omega_0 = \omega_s + \omega_p \\ k_0 = k_s + k_p\end{gathered} \tag{1.29}$$

, where subscripts 's', '0', and 'p' indicates scattered, incident and plasma waves, respectively.

Both of Eq. (1.29) are connected by the dispersion relationship, which has different forms depending on external conditions like plasma density, temperature, magnetic field, etc. The temperature condition gives the Bohm-Gross wave

$$\omega^2 = {\omega_p}^2 + \frac{3}{2}k^2 {v_{th}}^2 \tag{1.30}$$

, where v_{th} is the thermal velocity of electrons.

The external magnetic field condition gives alternative waves when the laser field is parallel to a magnetic field

$$\omega^2 = {\omega_p}^2 + c^2 k^2 \tag{1.31}$$

. This is so called 'O(Ordinary)-mode', which is the same as the case of a plasma density only. Alternatively, when the laser field is perpendicular to the magnetic field, the wave is given as

$$\frac{c^2k^2}{\omega^2} = 1 - \frac{{\omega_p}^2}{\omega^2}\frac{\omega^2 - {\omega_p}^2}{\omega^2 - {\omega_h}^2} \tag{1.32}$$

. This is so called ‘E(Extraordinary)-mode’.

The scattered wave can be expressed as a frequency shift of the incident wave (Fig. 1.3 (a)) and can be used for diagnosing various plasma specifications of density, temperature, and magnetic field.

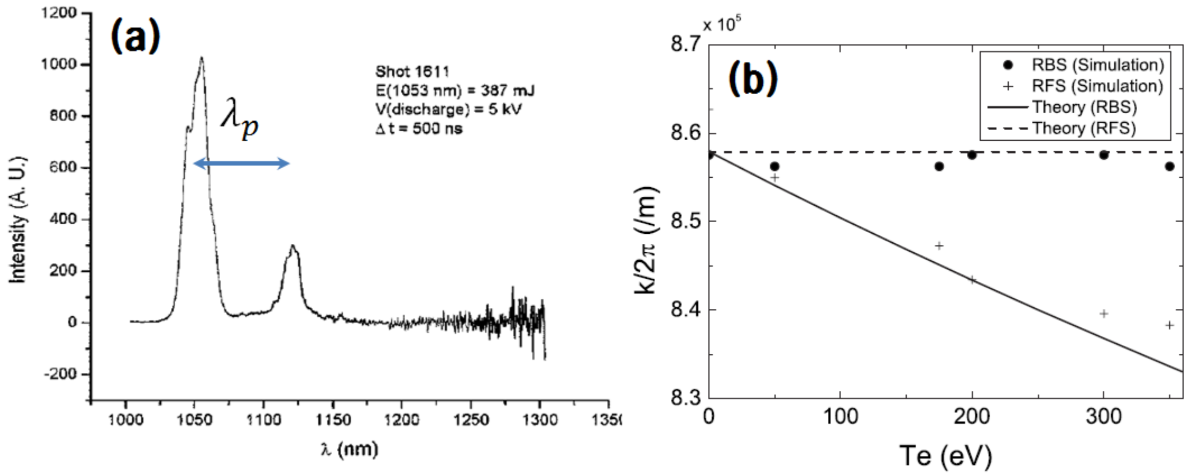

Figure 1.3 : (a) A typical backscattered spectrum from capillary discharge experiment. The central frequency indicates that the average interaction density is $1.5 \times 10^{18}\ \mathrm{cm}^{-3}$. [1]
(b) A forward and backward frequency shift in the amount of temperature dependency. [2]

The density case has the same frequency shift for the forward and backward scattering of the plasma frequency. In the temperature case, the frequency shifts the plasma frequency for the forward scattering which is the same as the density case. However, the backward case has a shifted frequency of the plasma frequency plus alpha which is dependent on temperature (Fig. 1.3 (b)). This is how the density and temperature of plasma can be predicted by measuring the frequency shift from the incident wave. The effect of magnetic fields will be studied in Chapter 4.

1.5 Ponderomotive force

When the high power laser is irradiated onto plasmas, the plasmas are affected by the radiation pressure, so called the *ponderomotive force*. As a kind of nonlinear or secondary motion of electrons the ponderomotive force can be derived from Maxwell’s equations and the Lorentz force. It is expressed as a time-averaged electron force.

Assuming a wave electric field of the form

$$E = E_s(r)e^{-i\omega t}, \tag{1.18}$$

the resultant ponderomotive force of one electron is [7]

$$F_p = -\frac{1}{4}\frac{e^2}{m\omega^2}\nabla {E_s}^2 = -\frac{1}{4}mc^2\nabla|a|^2 \tag{1.19}$$

, where a is the normalized vector potential.

When one laser propagates in plasmas, the ponderomotive force is

$$F_p = -\frac{1}{4}mc^2\nabla({a_0}^2) \tag{1.20}$$

, where $a = a_0(r)e^{ik\cdot r}$ in 3D. So the ponderomotive force is derived by the gradient of the laser pulse.

In the case of counter laser pulses, the ponderomotive force of laser collision is

$$\begin{aligned} F_p &= -\frac{1}{4}mc^2\nabla[(a_1 + a_2)(a_1 + a_2)^*] \\ &= -\frac{1}{4}mc^2\nabla\left({a_{1\_0}}^2 + {a_{2\_0}}^2\right) - \frac{1}{4}mc^2\nabla[a_1{a_2}^* + {a_1}^*a_2] \\ &= -\frac{1}{4}mc^2\nabla\left({a_{1_0}}^2 + {a_{2_0}}^2\right) - mc^2kRe[ia_1{a_2}^*]. \end{aligned} \tag{1.21}$$

Because the first term of Eq.(1.21) is very small compared to the second term due to wave number *k*, the ponderomotive is given as

$$F_p \approx -mc^2kRe[ia_1{a_2}^*]. \tag{1.22}$$

Usually when electrons oscillate following the laser’s field, the averaged electric force has nonlinear motion like the ponderomotive force. Eq. (1.22) is a useful expression for the Terahertz generation scheme in Chapter 3 and Eq. (1.20) is used for LWFA in Chapter 5.

Chapter 2

Particle In Cell (PIC) simulation

Theoretical studies on the laser-plasma interaction involve Maxwell’s equation and the force equation like the Lorentz force. For most of cases, finding solution of those equations is extremely hard. However, the numerical calculation offers the perfect solution and reduces the consumption of energy, time and efforts. Though plasma simulation methods have several classes such as kinetic, fluid, and hybrid method, I will treat PIC code as a kinetic method. A PIC code is composed of the field solver, applying the field value to each particle, the particle movement and the current calculation, which form one calculation loop [8]. Various techniques for the calculations can be imported in a code like a high order calculation, field ionization, PML, new field solver, and Lorentz boosted frame. Fig. 2.1 summarizes the calculation process.

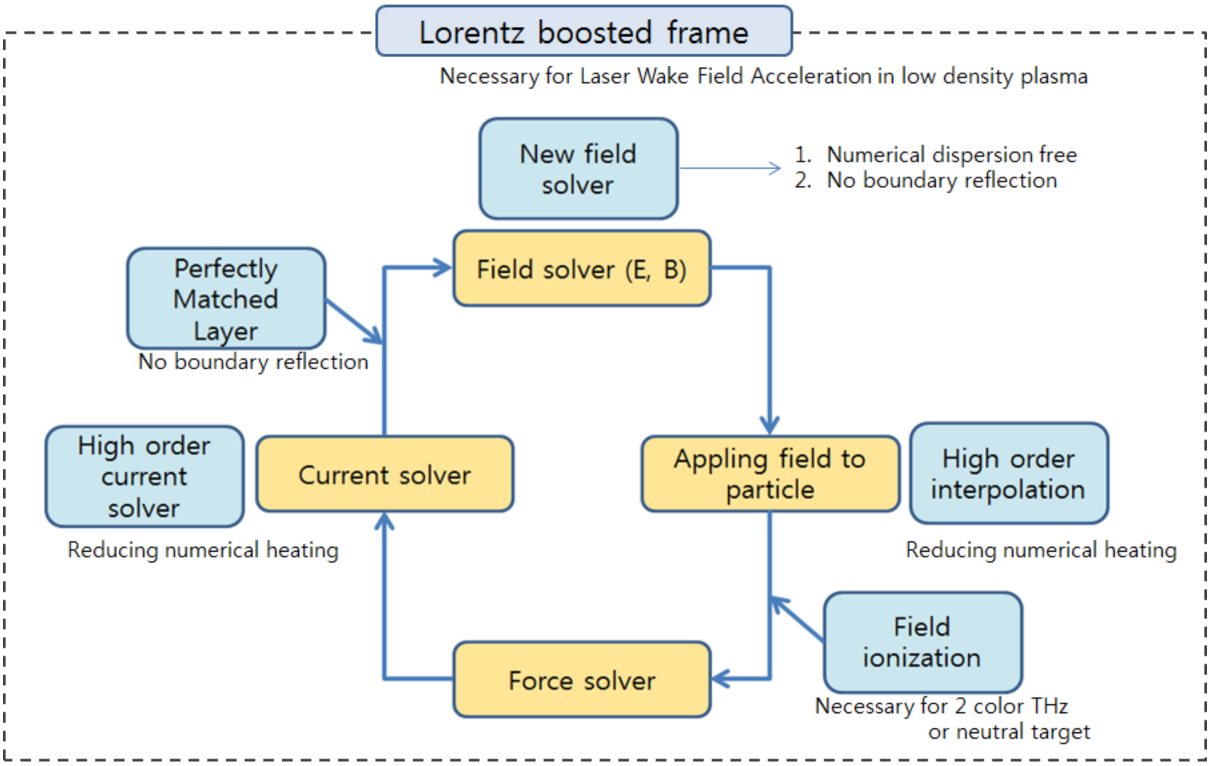

Figure 2.1 : The numerical loop for a PIC simulation methods with various techniques.

2.1 High order calculation

Because a calculation is performed on discretized mesh cells, the continuity is broken slightly during interpolating the fields to each particle, and the current calculation. Those make a kind of numerical errors which result in a numerical heating. Even though the numerical heating can be reduced by increasing resolution of meshes, heavy costs of calculation cannot be avoided. To reduce the numerical heating, the spline method can be a solution [9]. Using a high order spline method, errors can be reduced dramatically.

The main target of the spline method is to obtain the form factors of each adjacent mesh as shown in Fig. 2.2. 2D and 3D calculations are also just done by multiplying the form factor following y and z direction, so calculations become simpler than others interpolation methods like bi-cubic or tri-cubic spline. Because the sum of all adjacent mesh's form factors must be '*1*', multiplying 1D form factors of x, y and z coordinates also guarantees the sum as '*1*'. The interpolation is applicable for the part of applying field to particle and the calculating current.

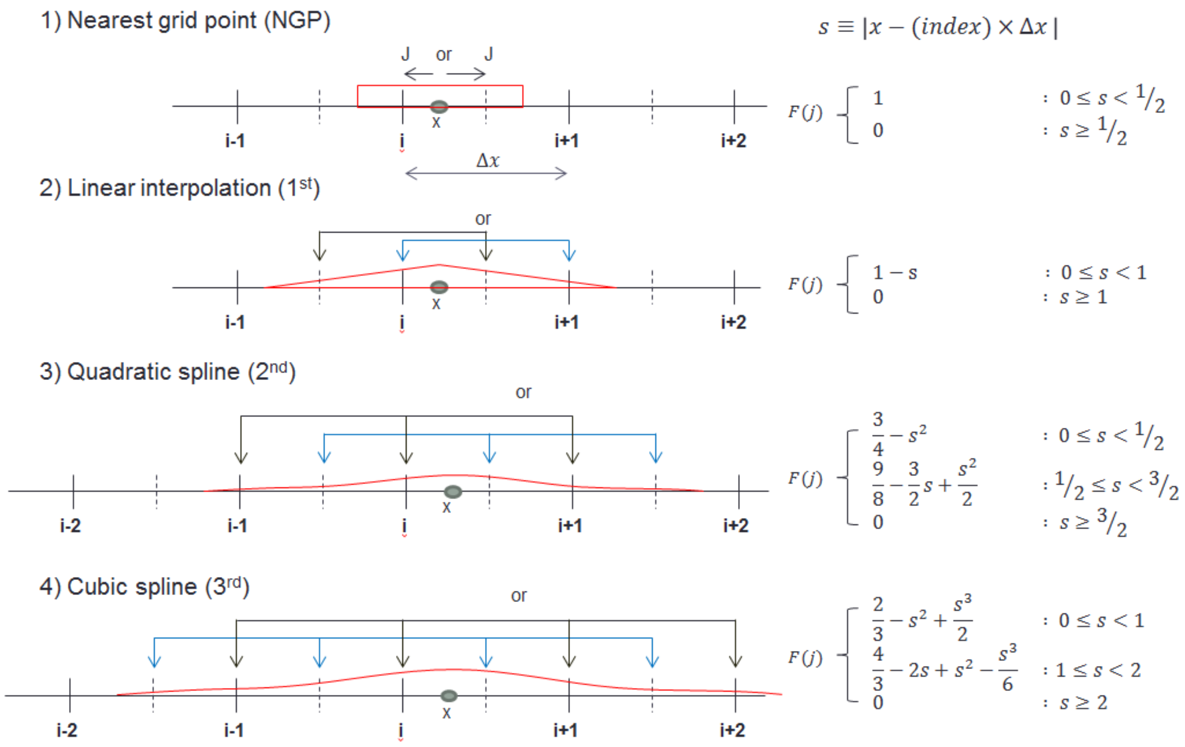

Figure 2.2 : 1D spline method with several orders of calculations.
$F(j)$ is the form factor and sum of $F(j)$ of adjacent meshes gives 1.

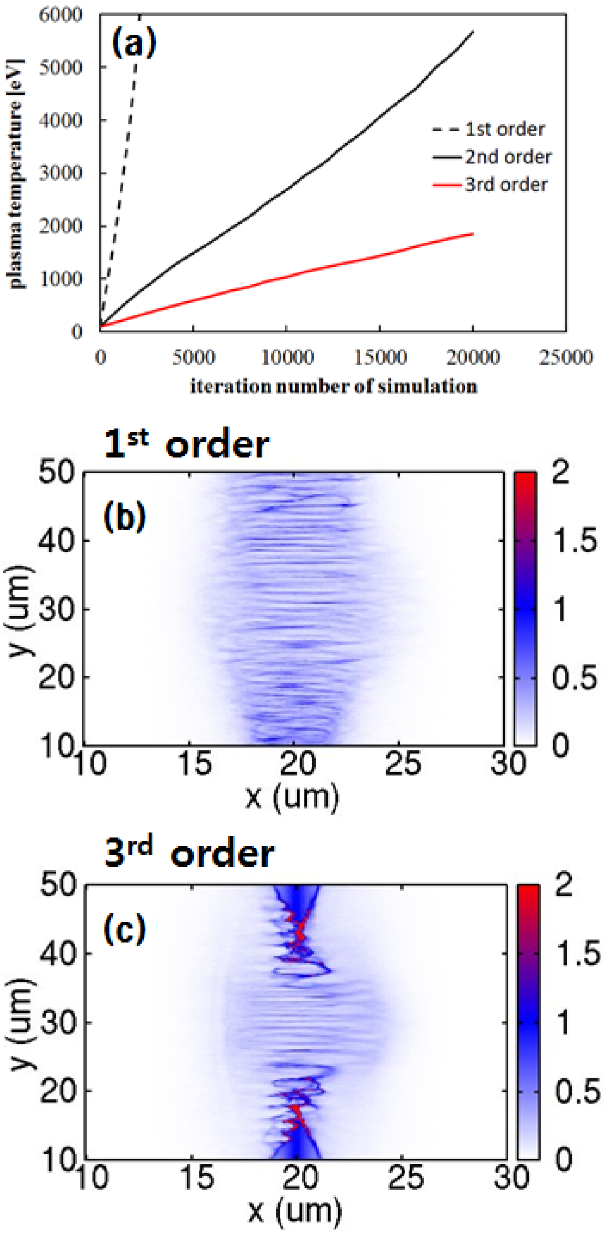

Figure 2.3 : (a) Numerical heating in different types of interpolation. Initial temperature of plasma is given as 100eV. Simulation parameters are $dx = {}^{\lambda}/_{20}$ $(\lambda = 1\mu m)$ and particle number in one cell is 2 at the plasma density $1.0 \times 10^{27} m^{-3}$. An example of ion acceleration with (b) 1st interpolation and (c) 3rd interpolation. Simulation parameters are the maximum plasma density $7.0 \times 10^{27} m^{-3}$, $dx = {}^{\lambda}/_{500}$ $(\lambda = 1\mu m)$ and particle number in one cell is 5.

For example, 2D current calculation of the 2nd order is done by following. The current function is given

$$\begin{aligned} J_x &= qnv_x \times f(j) \times g(i) \\ J_y &= qnv_y \times f(i) \times g(j) \\ J_z &= qnv_z \times f(i) \times f(j) \end{aligned} \tag{2.1}$$

, where i, j, f, and g are the index of x,y coordinate, quadratic, and linear spline form factor, respectively. As shown in Fig. 2.2, a linear spline uses 2 meshes *i.e.* i and $i+1$, however a quadratic spline needs 3 adjacent meshes *i.e.* $i-1$, i and $i+1$. Likewise, the 3rd order calculation has one-increased meshes.

Fig. 2.3 shows a numerical heating and an example of the ion acceleration with different order calculations. Real physical situations have a constant or decreasing temperature. When given initial temperature, however, Fig. 2.3(a) shows the increasing plasma temperature with time. So it is a non-physical situation. In Fig. 2.3(b), numerical errors exceed the laser field interaction, hence it is not clear to see the laser effect. However, Fig. 2.3(c) shows clear laser-plasma interaction like a hole boring.

2.2 New field solver (Field split method)

Though there are various numerical methods to solve Maxwell's equation, Yee solver has been thought as one of standard methods because of the simplicity of applications and the efficiency of low memory costs [10]. The original Yee solver has one problem of numerical dispersion of 2D and 3D calculations, which can arise in the direction of coordinate axes such as x, y and z [11]. To improve the numerical dispersion, several modified Yee solvers are introduced [12-14]. Here I will introduce 'Field Split Method' [8, 15].

In 2D, Maxwell's equation Eq. (1.2) and (1.3) can be rearranged as following:

$$\begin{aligned} \frac{\partial E_x}{\partial t} &= \frac{\partial B_z}{\partial y} - 2\pi J_x \\ \left(\frac{\partial}{\partial t} + \frac{\partial}{\partial x}\right) P_r &= \frac{1}{2}\frac{\partial E_x}{\partial y} - \pi J_y \\ \left(\frac{\partial}{\partial t} - \frac{\partial}{\partial x}\right) P_l &= -\frac{1}{2}\frac{\partial E_x}{\partial y} - \pi J_y \end{aligned} \tag{2.2}$$

, where $P_r = \left(E_y + B_z\right)/2$, $P_l = \left(E_y - B_z\right)/2$. All units are dimensionless by normalizing the time to $1/\omega_0$, the lengths to λ_0, the velocity to c, the electric field to $\mathrm{m}c\omega_0/e$, the magnetic field to $\mathrm{m}\omega_0/e$, and the current to en_0c.

The numerical equation of Eq. (2.2) is given as

$$
\begin{aligned}
{P_r}_{i+\frac{1}{2},j+\frac{1}{2}}^{n+\frac{1}{2}} &= {P_r}_{i-\frac{1}{2},j+\frac{1}{2}}^{n-\frac{1}{2}} + \frac{1}{2}\frac{\Delta t}{\Delta y}\left({E_x}_{i,j+1}^{n} - {E_x}_{i,j}^{n}\right) - \pi\Delta t {J_y}_{i,j+\frac{1}{2}}^{n} \\
{P_l}_{i-\frac{1}{2},j+\frac{1}{2}}^{n+\frac{1}{2}} &= {P_l}_{i+\frac{1}{2},j+\frac{1}{2}}^{n-\frac{1}{2}} - \frac{1}{2}\frac{\Delta t}{\Delta y}\left({E_x}_{i,j+1}^{n} - {E_x}_{i,j}^{n}\right) - \pi\Delta t {J_y}_{i,j+\frac{1}{2}}^{n} \\
{E_x}_{i,j}^{n+1} &= {E_x}_{i,j}^{n} + \frac{\Delta t}{2\Delta y}\left({B_z}_{i+\frac{1}{2},j+\frac{1}{2}}^{n+\frac{1}{2}} + {B_z}_{i-\frac{1}{2},j+\frac{1}{2}}^{n+\frac{1}{2}} - {B_z}_{i+\frac{1}{2},j-\frac{1}{2}}^{n+\frac{1}{2}} - {B_z}_{i-\frac{1}{2},j-\frac{1}{2}}^{n+\frac{1}{2}}\right) \\
&\quad - \pi\Delta y\left({J_x}_{i+\frac{1}{2},j}^{n+\frac{1}{2}} + {J_x}_{i-\frac{1}{2},j}^{n+\frac{1}{2}}\right) \\
{P_r}_{i+\frac{1}{2},j+\frac{1}{2}}^{n+1} &= {P_r}_{i-\frac{1}{2},j+\frac{1}{2}}^{n} + \frac{1}{2}\frac{\Delta t}{\Delta y}\left({E_x}_{i,j+1}^{n+\frac{1}{2}} - {E_x}_{i,j}^{n+\frac{1}{2}}\right) - \pi\Delta t {J_y}_{i,j+\frac{1}{2}}^{n+\frac{1}{2}} \\
{P_l}_{i-\frac{1}{2},j+\frac{1}{2}}^{n+1} &= {P_l}_{i+\frac{1}{2},j+\frac{1}{2}}^{n} - \frac{1}{2}\frac{\Delta t}{\Delta y}\left({E_x}_{i,j+1}^{n+\frac{1}{2}} - {E_x}_{i,j}^{n+\frac{1}{2}}\right) - \pi\Delta t {J_y}_{i,j+\frac{1}{2}}^{n+\frac{1}{2}} \\
{E_x}_{i,j}^{n+\frac{1}{2}} &= {E_x}_{i,j}^{n-\frac{1}{2}} + \frac{\Delta t}{2\Delta y}\left({B_z}_{i+\frac{1}{2},j+\frac{1}{2}}^{n} + {B_z}_{i-\frac{1}{2},j+\frac{1}{2}}^{n} - {B_z}_{i+\frac{1}{2},j-\frac{1}{2}}^{n} - {B_z}_{i-\frac{1}{2},j-\frac{1}{2}}^{n}\right) \\
&\quad - \pi\Delta y\left({J_x}_{i+\frac{1}{2},j}^{n} + {J_x}_{i-\frac{1}{2},j}^{n}\right)
\end{aligned}
\tag{2.3}
$$

, where *n* is the index of time step. These are for description of P polarized field calculation. As shown in Eq.(2.2), the calculation is done in 2 steps for one simulation time step. Note that the current memories become double compared with Yee mesh solver.

The S Polarized field is also obtainable similarly

$$
\begin{gathered}
\frac{\partial B_x}{\partial t} = \frac{\partial E_z}{\partial y} \\
\left(\frac{\partial}{\partial t} - \frac{\partial}{\partial x}\right) S_l = -\frac{1}{2}\frac{\partial B_x}{\partial y} - \pi J_z \\
\left(\frac{\partial}{\partial t} + \frac{\partial}{\partial x}\right) S_r = -\frac{1}{2}\frac{\partial B_x}{\partial y} - \pi J_z
\end{gathered}
\tag{2.4}
$$

, where $S_l = \left(E_z + B_y\right)/2,\ P_l = \left(E_z - B_y\right)/2$. The numerical equations of Eq. (2.4) are given as following

$$
\begin{aligned}
S_{r\,i+\frac{1}{2},j+\frac{1}{2}}^{\;n+\frac{1}{2}} &= S_{r\,i-\frac{1}{2},j+\frac{1}{2}}^{\;n-\frac{1}{2}} - \frac{1}{2}\frac{\Delta t}{\Delta y}\left(B_{x\,i,j+1}^{\;n} - B_{x\,i,j}^{\;n}\right) - \frac{\pi}{2}\Delta t\left(J_{z\,i,j+1}^{\;n} + J_{z\,i,j}^{\;n}\right)\\
S_{l\,i-\frac{1}{2},j+\frac{1}{2}}^{\;n+\frac{1}{2}} &= S_{l\,i+\frac{1}{2},j+\frac{1}{2}}^{\;n+\frac{1}{2}} - \frac{1}{2}\frac{\Delta t}{\Delta y}\left(B_{x\,i,j+1}^{\;n} - B_{x\,i,j}^{\;n}\right) - \frac{\pi}{2}\Delta t\left(J_{z\,i,j+1}^{\;n} + J_{z\,i,j}^{\;n}\right)\\
B_{x\,i,j}^{\;n+1} &= B_{x\,i,j}^{\;n} - \frac{\Delta t}{2\Delta y}\left(E_{z\,i+\frac{1}{2},j+\frac{1}{2}}^{\;n+\frac{1}{2}} + E_{z\,i-\frac{1}{2},j+\frac{1}{2}}^{\;n+\frac{1}{2}} - E_{z\,i+\frac{1}{2},j-\frac{1}{2}}^{\;n+\frac{1}{2}} - E_{z\,i-\frac{1}{2},j-\frac{1}{2}}^{\;n+\frac{1}{2}}\right)\\
S_{r\,i+\frac{1}{2},j+\frac{1}{2}}^{\;n+1} &= S_{r\,i-\frac{1}{2},j+\frac{1}{2}}^{\;n} - \frac{1}{2}\frac{\Delta t}{\Delta y}\left(B_{x\,i,j+1}^{\;n+\frac{1}{2}} - B_{x\,i,j}^{\;n+\frac{1}{2}}\right) - \frac{\pi}{2}\Delta t\left(J_{z\,i,j+1}^{\;n+\frac{1}{2}} + J_{z\,i,j}^{\;n+\frac{1}{2}}\right)\\
S_{l\,i-\frac{1}{2},j+\frac{1}{2}}^{\;n+1} &= S_{l\,i+\frac{1}{2},j+\frac{1}{2}}^{\;n} - \frac{1}{2}\frac{\Delta t}{\Delta y}\left(B_{x\,i,j+1}^{\;n+\frac{1}{2}} - B_{x\,i,j}^{\;n+\frac{1}{2}}\right) - \frac{\pi}{2}\Delta t\left(J_{z\,i,j+1}^{\;n+\frac{1}{2}} + J_{z\,i,j}^{\;n+\frac{1}{2}}\right)\\
B_{x\,i,j}^{\;n+\frac{1}{2}} &= B_{x\,i,j}^{\;n-\frac{1}{2}} - \frac{\Delta t}{2\Delta y}\left(E_{z\,i+\frac{1}{2},j+\frac{1}{2}}^{\;n} + E_{z\,i-\frac{1}{2},j+\frac{1}{2}}^{\;n} - E_{z\,i+\frac{1}{2},j-\frac{1}{2}}^{\;n} - E_{z\,i-\frac{1}{2},j-\frac{1}{2}}^{\;n}\right).
\end{aligned}
\tag{2.5}
$$

The subscriptions of ‘r’ and ‘l’ of $P_r, P_l, S_r,$ and S_l indicate ‘right’ and ‘left’, respectively. The numerical equations Eq. (2.3) and (2.5) address that the field values of a whole mesh are just moved to the next grid points in each simulation time step. This transferring field information has an advantage of numerical dispersion as free. Maxwell’s equation can also be expanded in P_u and P_d such as ‘up’ and ‘down’. These mean the propagating direction of field, so the method is called ‘directional split’ or ‘field split’. Even though the cell size is large, because the calculation is done by transferring field values, the distortion of laser field does not happen. Moreover, it does not give a field reflection at the simulation boundary, so it does not need PML boundary. For these reasons this method is used for the scattering problem (Chapter 4). Fig. 2.4 is an example of Field split method.

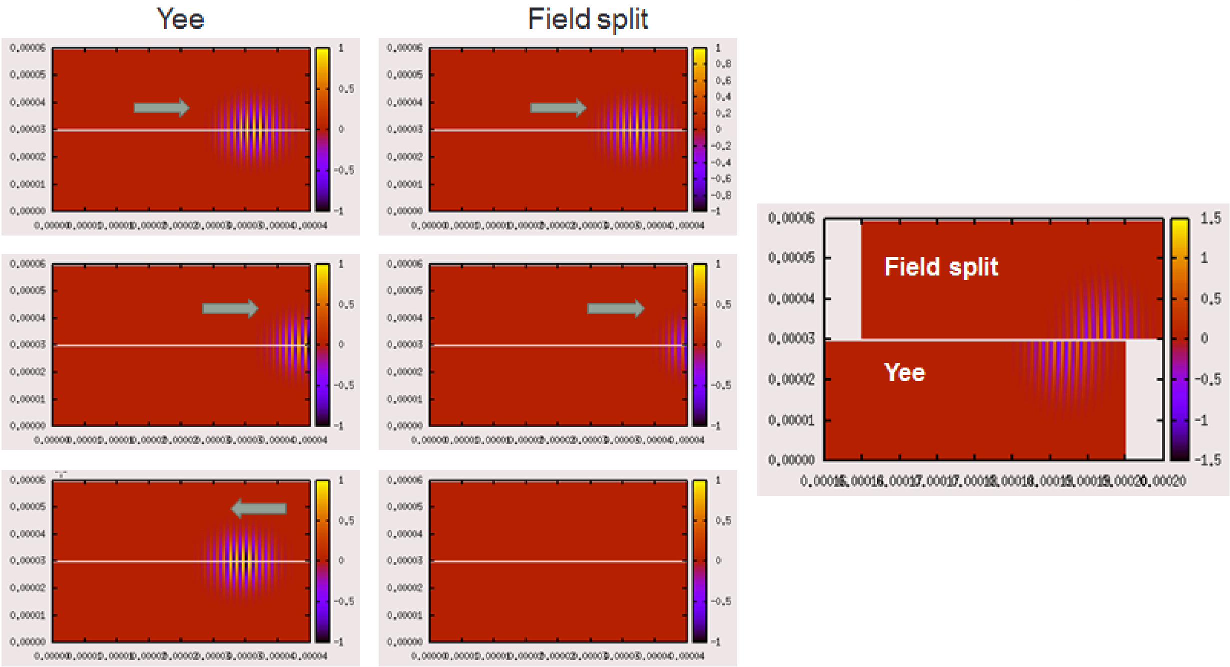

Figure 2.4 : Comparison between Yee and Field split method. Field split method does not have field reflection at the boundary. When running significantly long distance, Yee solver reveals retarded propagation, however Field split method has numerical dispersion free.

2.3 Lorentz boosted frame

Lorentz boosted frame was developed for particular cases of particle acceleration. Being contrast to traditional simulations of the view of lab frame, this frame works on the view of the moving frame following accelerated particles. Because Maxwell's equation and the Lorentz force keep their forms in the boosted frame, the simulation process does not need to change its own procedure except of initial simulation settings such as a laser frequency, cell size, simulation's domain size and plasma conditions. Table 1.1 is the comparison of initial parameter settings between the lab frame and the boosted frame. The boosted frame can reduce the simulation time significantly [11, 16, 17] with tens of simulation speed, so it now has become an important simulation technique especially in the field of Laser Wake Field Acceleration (LWFA) and Particle driven Wake Field Acceleration (PWFA). Since the simulation size is affected by the plasma wave length, when doing in lower plasma density, it needs bigger simulation domain size. For example, when it is done for 3D simulation of the plasma density $1.0 \times 10^{25} m^{-3}$ and 1mm propagation, the case of $1.0 \times 10^{24} m^{-3}$ would need 37-fold simulation time!

	Lab frame	**Boosted frame**
Wave length	λ	$\gamma(1+\beta)\lambda$
Wave frequency	ω	$\omega/\gamma(1+\beta)$
Cell size	dx	$\gamma(1+\beta)dx$
Time step	dt	$\gamma(1+\beta)dt$
Laser amplitude	a_0	$a_{0/\gamma(1+\beta)}$
Domain size	D	$\gamma(1+\beta)D$
Plasma density	n_0	γn_0
Plasma velocity	*0*	$-c\beta$
Plasma length or position	$L\ or\ x$	$L/\gamma\ or\ x/\gamma$

Table 1.1 The parameter comparison between lab frame and boost frame.
γ is moving frame's relativistic gamma factor.

Even though the process of boosted frame is the same as the lab frame calculation, the backward signal field has significant noises and the reasons are given as following. From the Lorentz transform,

$$E_y' = \gamma\left(E_y - vB_z\right) \tag{2.6}$$

, when the field goes backward, the magnetic field becomes as

$$B_z = -\frac{E_y}{c} \quad \left(forward\ case\ is\ B_z = \frac{E_y}{c}\right). \tag{2.7}$$

Then Eq. (2.6) has the form

$$E_y' = \gamma(1+\beta)E_y. \tag{2.8}$$

As described in Eq. (2.8), the amplitude of backward fields diverse with simulation time.

To delete this noise, the binomial filtering method was used [11, 18] as following.

$$\Phi_i = \alpha\varphi_i + (1-\alpha)\frac{\varphi_{i-1} + \varphi_{i+1}}{2} \tag{2.9}$$

$when\ \alpha$=0.5, $smoothening\ (filtering)$

$when\ \alpha$=1.5, $compensation\ (compensating\ lowered\ value\ by\ smoothening)$

When doing *filtering i.e.* α=0.5, original fields lose their own values slightly. When doing the calculation with α=1.5, it compensates lost values. Therefore as a final filter function, combination of the filtering and the compensation was used.

$$F_i = \Phi_i(\alpha = 0.5)\Phi_i(\alpha = 1.5). \tag{2.10}$$

Fig. 2.5 shows an example of filtering 1D calculation.

The last thing for the boosted frame is to convert data from the boosted frame to the lab frame. Here is useful Lorentz transform for converting data.

$$\begin{gathered} t' = \gamma\left(t - \frac{\beta}{c}x\right) \\ x' = \gamma(x - vt) \\ y' = y \\ z' = z \end{gathered} \tag{2.11}$$

$$\begin{gathered} E_x' = E_x \\ E_y' = \gamma(E_y - vB_z) \\ E_z' = \gamma(E_z + vB_y) \\ B_x' = B_x \\ B_y' = \gamma\left(B_y + \frac{\beta}{c}E_z\right) \\ B_z' = \gamma\left(B_z - \frac{\beta}{c}E_y\right) \end{gathered} \tag{2.12}$$

To obtain values for a certain lab frame time, it needs information of different time steps in boosted frame. It need to find the profit x position corresponding to the targeted lab frame time in every time step using Eq. (2.11). Then the result data is completed by gathering all field information using Eq. (2.12). Particle or density data is also obtainable using Eq. (2.11) and proper Lorentz transformation. Fig. 2.6 is an example of 1D boosted frame.

2D or 3D calculation is also same as 1D except for treating laser, because of transversal space component such as y and z direction. The method for multi-dimension’s laser treatment is introduced in Ref. [17].

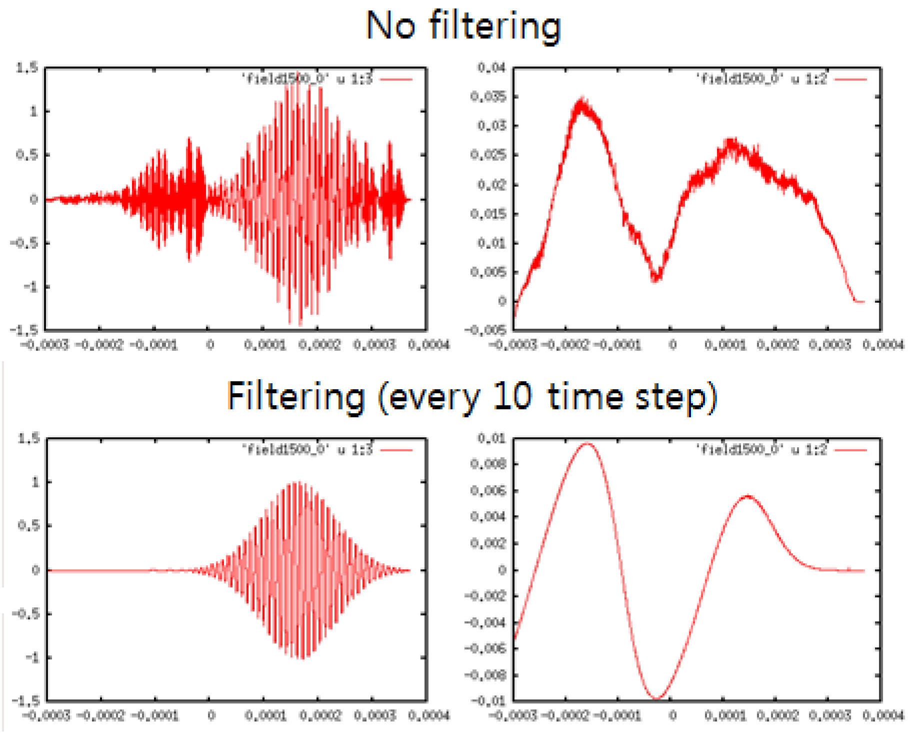

No filtering

Filtering (every 10 time step)

Figure 2.5 : The example of binomial filtering by Eq. (2.9).

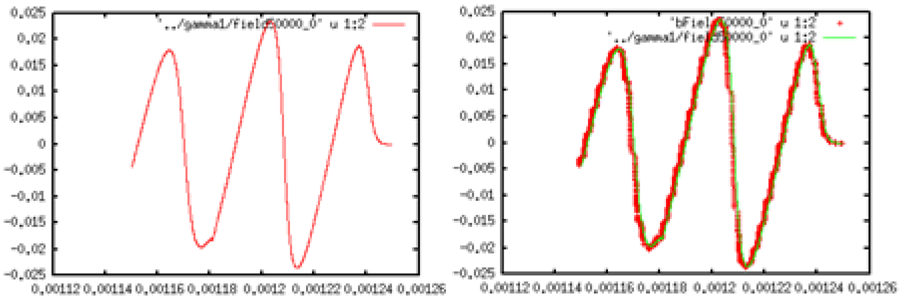

Lab frame ($\gamma = 1$)
25m34s

$\gamma = 5$
Filtering step 10
48s

Figure 2.6 : Simulation of boosted frame and lab frame in 1D after 50000 time step. When $\boldsymbol{\gamma} = \mathbf{5}$, simulation speed was 31 times faster than lab frame.

2.4 Field ionization

When a high power laser passes neutral gas, the plasma is generated by ionization from the laser field. Sometimes the simulation results between ionization and non-ionization are quite different. Especially the field ionization method is important for the 2 color laser scheme [19] for Terahertz generation and ion target acceleration. Although there are other field ionization theories, I used ADK model [20] which is assumed that atoms are hydrogen-like. This model shows the ionization rate for one electron, so using the ionization rate the electrons and ions are generated every simulation time step from given ionization energies. The ionization rate has the form

$$\omega_{ADK}[s^{-1}] = \omega_a \frac{1}{8\pi Z}\frac{E}{E_a}\left(4e\frac{Z^3}{n^*}\frac{E_a}{E}\right)^{2n^*} exp\left[-\frac{2}{3}\frac{E_a}{E}\left(\frac{U_i}{U_H}\right)^{3/2}\right] \tag{2.13}$$

, where $\omega_a = 4.134 \times 10^{16}[s^{-1}]$, $E_a = 5.142 \times 10^{11}[V/m]$, ionization energy of Hydrogen $U_H = 2.180 \times 10^{-18}[J]$, euler number $e = 2.718$, ion number Z and effective quantum number $n^* = Z/\sqrt{U_i/U_H}$. Table 2.1 is a useful ionization energy table.

Atom	Ion number							
	1	2	3	4	5	6	7	8
H	13.6							
He	24.6	54.4						
Li	5.4	75.6	122.4					
Be	9.3	18.2	153.9	217.7				
B	8.3	25.1	37.9	259.3	340.2			
C	11.3	24.4	47.9	64.5	392.0	489.8		
N	14.5	29.6	47.4	77.5	97.9	551.9	666.8	
O	13.6	35.1	54.9	77.4	113.9	138.1	739.2	871.3
F	17.4	35.0	62.7	87.1	114.2	157.1	185.1	953.6
Ne	21.6	41.1	63.5	97.0	126.2	158.0		
Na	5.1	47.3	71.6	98.9	138.4	172.0	208.5	266.0
Mg	7.6	15.0	80.1	109.3	141.2	186.5	224.9	266.0

Table 2.1 Ionization table [eV]

Chapter 3

Terahertz radiation by colliding lasers in magnetized plasmas

1. Introduction

Far-infrared light sources have long been the poor relation of electromagnetic sources for probing and imaging the structure and dynamics of matter. Enormous effort is now being made to fill the perceived terahertz (THz) gap, with the development of high power THz sources, because of their potential high impact applications in science and technology. Diverse sources have been developed using both electronic and optical methods, for example the laser-plasma-based schemes [19, 21-38] which promise compact THz sources with notably high field amplitude over a wide range of frequencies, and conventional beam driven vacuum sources such as gyrotrons, backward wave oscillators etc.

Linear mode conversion [28, 39] and the two-color schemes are known to yield short duration and wide-band THz pulses with remarkably high amplitude, up to MV/cm level. The latter is attractive because of its high conversion efficiency and moderate laser requirement [34, 35].

While the peak power of these wide band THz sources is increasing rapidly, the average power of available narrow band THz sources remains very low. A monochromatic THz source based on laser-plasma interactions and wake fields is feasible [25]. By converting the longitudinal current of the wake field to a transverse one using an external magnetic field, this Cherenkov wake scheme may extend the pulse duration and increase the emission power [36-38]. However, the field amplitude or power from such a monochromatic THz source is still low, compared with wide-band schemes. Considering the numerous important applications such as the high-contrast imaging [40-42] or the interferometry of Tokamak plasmas [43, 44], it is necessary to provide suitable monochromatic sources that have high tunability, compactness, and most of all high power.

In this chapter, it is proposed a new mechanism of generating high intensity and monochromatic THz radiation from laser-plasma interactions. The fundamental idea is to evoke a strong, localized, long-lasting electron oscillation in plasma, which acts as a radiating antenna emitting a continuous THz wave. Practically the radiation current source can be generated by the strong ponderomotive force from two short laser pulses colliding at a desired position inside the plasma [44]. Then the longitudinal oscillation induced in this way is converted to a transverse one by a weak transverse external magnetic field. Because the radiation from this current source oscillates at the plasma frequency, the electromagnetic fields are usually cut-off by the ambient plasma in a normal condition, which is indeed the very reason why plasma oscillations cannot be easily converted to transverse electromagnetic waves in laser-plasma systems. However, it has been discovered that when electromagnetic wave is constantly driven near cut-off, as in this case, the field grows as its energy is fed by the driving current. Furthermore, both electric and magnetic components of the field diffuse strongly into the plasma. As a consequence, the diffusing electromagnetic field eventually propagates across the plasma-vacuum boundary and is converted to an emitted electromagnetic wave into free space. This concept of THz generation is shown schematically in Fig. 2.1.

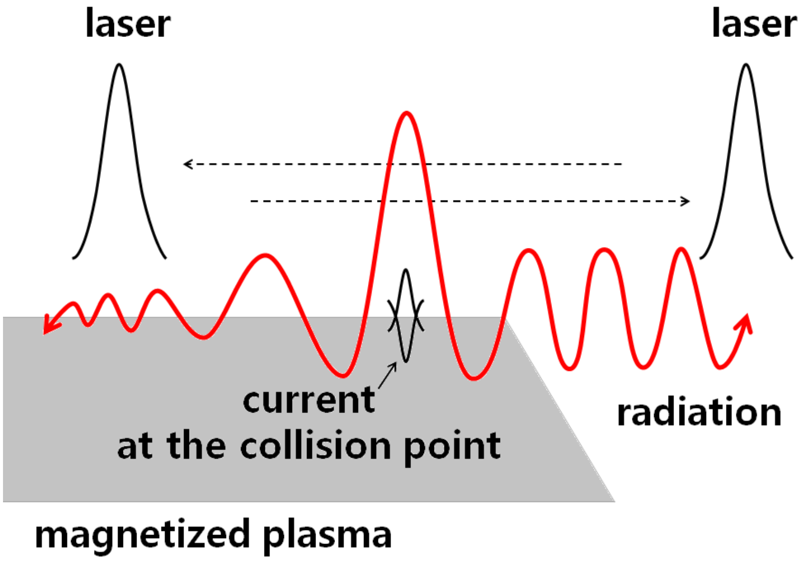

Figure 3.1 : Schematic of terahertz emission from a current source generated by two counter-propagating laser pulses.

As the plasma frequency can be easily controlled in the few THz regime, this mechanism can be utilized as a new THz radiation source. As I will show later through numerical simulations, the resultant amplitudes of the THz emission reach tens of MV/m and has a sub-nano-second pulse duration. Such high amplitude and long duration waves in the few THz frequency regime cannot be readily obtained using conventional methods in compact systems.

2. Electromagnetic diffusion and growing near cut-off frequency

The diffusion of the electromagnetic field, which is a key factor for enhanced THz emission in this scheme, is apparent in the field evolution modelled by a constantly driven complex diffusion equation. Such diffusion of the electromagnetic wave is quite different from the well-known magnetic field diffusion into conducting material, where just the slowly varying magnetic component diffuses while the electric component remains negligibly small. To describe electromagnetic diffusion near cut-off, we start from the wave equation:

$$\begin{aligned}\frac{\partial^2 E_y}{\partial \mathrm{x}^2}-\frac{1}{c^2}\frac{\partial^2 E_y}{\partial \mathrm{t}^2}=\frac{4\pi}{c^2}\frac{\partial J_y}{\partial t}\\ =\frac{4\pi}{c^2}\frac{\partial}{\partial t}\left(-n_0 e v_y+\hat{J}_0 e^{-i\omega t}\right)\\ =\frac{4\pi}{c^2}\frac{\partial}{\partial t}\left(-n_0 e\frac{-eE_y}{m}+\hat{J}_0 e^{-i\omega t}\right)\\ =\frac{{\omega_p}^2}{c^2}E_y+\frac{\partial}{\partial t}\left(\hat{J}_0 e^{-i\omega t}\right)\end{aligned} \tag{3.1}$$

Note that the first term on the right-hand-side is the self-current induced by E_y itself, while the second term is a constant driving current. By assuming that the electric field amplitude evolves slowly, the electric field E_y can be written as $\hat{E}e^{-i\omega t}$, where $\hat{E}$ is a slowly evolving function of time. Since $\omega \cong \omega_p$, *i.e.* E_y is nearly at cut-off, the first term on the right-hand-side is cancelled out by the second time derivative of $e^{-i\omega t}$ on the left-hand-side. Neglecting the second time derivative of $\hat{E}$ from the slowly varying assumption, we obtain a constantly driven diffusion-like equation of the electric field:

$$\frac{\partial^2 \hat{E}}{\partial \mathrm{x}^2}+\frac{i2\omega_p}{c^2}\frac{\partial^2 \hat{E}}{\partial \mathrm{t}^2}=-\frac{i4\pi\omega_p}{c^2}\hat{J}_0(x) \tag{3.2}$$

Note that Eq. (3.2) takes the usual form of a driven diffusion equation, except that the diffusion coefficient, which is $-\mathrm{i}c^2/2\omega_p$, is complex.

From the Laplace transform

$$f(t)=\int_0^\infty \hat{f}(t)e^{-st}dt, \tag{3.3}$$

Eq. (3.2) has the form of

$$\frac{\partial^2 \mathrm{E}}{\partial \mathrm{x}^2}+\frac{i2s\omega_p}{c^2}\mathrm{E}=-\frac{i4\pi\omega_p}{sc^2}J_0(x). \tag{3.4}$$

If all variables are normalized by the value corresponding to ω_p (refer to Chapter1 1.1), Eq. (3.4) becomes

$$\frac{\partial^2 a_p}{\partial \xi^2}+\frac{i2s}{\omega_p}a_p=-\frac{i}{s}j_0(\xi) \tag{3.5}$$

, where ξ is the normalized length and a_p is the normalized vector potential. Using Green function method

$$\left(\frac{d^2}{dx^2}+k^2\right)\mathrm{G}(x-x')=-\delta(x-x') \;\Rightarrow \mathrm{G}(x-x')=\frac{i}{2k}e^{ik|x-x'|}, \tag{3.6}$$

to solve Eq. (3.5), the solution of Eq. (3.5) is

$$a_p(s) = -\sqrt{\frac{\omega_p}{2i}}\frac{1}{2s^{3/2}}\int_{-\infty}^{\infty} e^{i\mu|\xi-\xi'|} j_0 d\xi' \tag{3.7}$$

$$\mu \equiv \sqrt{2is/\omega_p}.$$

And using inverse Laplace transform

$$\hat{f}(t) = \frac{1}{2\pi i}\int_{\gamma-i\infty}^{\gamma+i\infty} e^{st} f(t) ds, \tag{3.8}$$

The final solution of Eq. (3.2) can be represented as follows:

$$\hat{a}_p(\xi,\tau) = \frac{1+i}{8\pi}\int_{-\infty}^{\infty} d\xi' \hat{j}_0 e^{-|\xi-\xi'|^2/\sigma^2}\int_{\gamma-i\infty}^{\gamma+i\infty} ds \frac{e^{s\tau+i\sqrt{2is}|\xi-\xi'|}}{s^{3/2}} \tag{3.9}$$

, where τ is the normalized time and the current is assumed as $\hat{j}_0(\xi) = \hat{j}_0 e^{-\xi^2/\sigma^2}$. Approximated solutions of Eq. (3.9) can be obtained by using the steepest descent method (saddle point method) as follows

$$p(s) \equiv s\tau + i\sqrt{2is}|\xi-\xi'|, \tag{3.8}$$

$$p(s_0)' = 0 \;\; \Rightarrow \;\; s_0 = \frac{|\xi-\xi'|^2}{i2\tau^2}, \tag{3.9}$$

$$p(s_0)'' = \frac{\tau^3}{|\xi-\xi'|^3} e^{i\pi/2}. \tag{3.10}$$

To avoid the rising area of complex plane, the phase direction is chosen by the steepest descent argument

$$\mathrm{z} = z_0 + T\mathrm{e}^{\mathrm{i}\alpha} \tag{3.11}$$

$$\alpha = \frac{\pi}{2} - \frac{1}{2} arg[p(s_0)''] = \frac{\pi}{4}, \tag{3.12}$$

then ***‘s’*** becomes

$$\mathrm{s} \approx s_0 + Te^{i\pi/4}, \tag{3.13}$$

and $p(s)$ is

$$p(s) \approx i\frac{|\xi-\xi'|^2}{2\tau} - \frac{\tau^3}{2|\xi-\xi'|^2}T^2. \tag{3.14}$$

The approximated form of Eq. (2.9) is represented as

$$\hat{a}_p(\xi,\tau)$$

$$= \frac{\sqrt{2}}{8\pi} e^{i\pi/2} \int_{-\infty}^{\infty} d\xi' \hat{j}_0 e^{-\xi'^2/\sigma^2} e^{i|\xi-\xi'|^2/2\tau} \int_{-\infty}^{\infty} dT \frac{e^{\frac{\tau}{2}\left(-\frac{\tau^2}{|\xi-\xi'|^2}\right)}}{\frac{|\xi-\xi'|^3}{\sqrt{2i}^3}\left(1+\frac{\sqrt{2i}\tau}{|\xi-\xi'|} T e^{i\pi/4}\right)^{3/2}}. \tag{3.17}$$

More reduced form of Eq. (3.17) can be obtained in certain limits. First, for $|\xi-\xi'|/\tau \gg 1$, *i.e.* far from the current source position and temporally in the early stage which leads to

$$\hat{a}_p(\xi,\tau) = -\frac{\sigma \hat{j}_0}{\sqrt{2}} \frac{\tau^{3/2}}{\xi^2} cos\left(\frac{\xi^2}{2\tau}+\frac{\pi}{4}\right). \tag{3.18}$$

Second, for $=0$, *i.e.* at the oscillation center of the current, Eq. (3.17) is represented as follows, which have assumptions of $\frac{|\xi-\xi'|}{\tau} = 1$ because the wave propagates the distance ξ' with time τ after colliding laser each other

$$\hat{a}_p(0,\tau) = \frac{\sqrt{2}}{8\pi} e^{\frac{i\pi}{2}} \sqrt{2i}^3$$
$$\times \int_{-\infty}^{\infty} d\xi' \hat{j}_0 e^{-\frac{\xi'^2}{\sigma^2}} e^{\frac{i\xi'}{2}} \left[\int_{-\infty}^{0} dT \frac{e^{-\frac{\tau}{2}T^2}}{\left(1+\sqrt{2i}T\right)^{3/2}} + \int_{0}^{\infty} dT \frac{e^{-\frac{\tau}{2}T^2}}{\left(1+\sqrt{2i}T\right)^{3/2}}\right] \tag{3.19}$$

$$= \frac{\sqrt{2}}{8\pi} e^{\frac{i\pi}{2}} \sqrt{2i}^3 \int_{-\infty}^{\infty} d\xi' \hat{j}_0 e^{-\left(\frac{\xi'^2}{\sigma^2}-\frac{i\xi'}{2}\right)}$$
$$\times \sqrt{\frac{\tau}{2}} \int_0^{\infty} \left[\frac{e^{-y}}{\left(1-i\frac{2}{\sqrt{\tau}}y^{1/2}\right)^{3/2}} + \frac{e^{-y}}{\left(1+i\frac{2}{\sqrt{\tau}}y^{1/2}\right)^{3/2}}\right] y^{-1/2} dy \tag{3.20}$$

, where $y \equiv \frac{\tau}{2}T^2$. When assuming early stage (τ is relatively small), the terms in bracket of Eq.(3.20) can be expanded with the orders of y

$$\begin{aligned} y^{-1/2}\left(1-i\frac{2}{\sqrt{\tau}}y^{1/2}\right)^{-3/2} &\approx y^{-1/2}\left(1-\frac{3}{2}i\frac{2}{\sqrt{\tau}}y^{1/2}+\cdots\right) \\ y^{-1/2}\left(1+i\frac{2}{\sqrt{\tau}}y^{1/2}\right)^{-3/2} &\approx y^{-1/2}\left(1+\frac{3}{2}i\frac{2}{\sqrt{\tau}}y^{1/2}+\cdots\right). \end{aligned} \tag{3.21}$$

So $n=1$ terms are deleted. Using Watson lemma

$$f(t) \sim \sum_{n=0}^{\infty} a_n t^{\lambda_n - 1} \tag{3.22}$$

$$\int_0^\infty e^{-zt} f(t)dt \sim \sum_{n=0}^{\infty} a_n \frac{\Gamma(\lambda_n)}{z^{\lambda_n}}$$

, where $\lambda_n > 0,\ n = 0$ term becomes

$$\int_0^\infty e^{-y} y^{-1/2} \left(1 - i\frac{2}{\sqrt{\tau}} y^{1/2}\right)^{-3/2} dy \sim \frac{\Gamma(\lambda_0)}{(1)^{\lambda_0}} = \Gamma\left(\frac{1}{2}\right) = \sqrt{\pi}. \tag{3.23}$$

Consequently Eq. (3.20) is reduced to an asymptotic form as a function of τ as follows

$$\hat{a}_p(0,\tau) = -(1+i)\frac{\hat{j}_0\sigma}{2}\sqrt{\tau}e^{-\sigma^2/16}. \tag{3.24}$$

Fig. 3.2 (a) is snapshot of the diffusing fields at different time, obtained from numerical integration of Eq. (3.2). As the field diffuses, its modulation length shrinks with increasing distance for fixed time, while growing at a fixed position as can be predicted from the cosine term in Eq. (3.18). Such a temporal behavior is presented in Fig. 3.2 (b), where the numerical integration of Eq. (3.2) is plotted at $\omega_p x/c = 0$ (current center), 5, and 10. The central field increases monotonically by $\sqrt{t}$ as expected from Eq. (3.24), while the off-central field initially follows $\mathrm{t}^{3/2}$ obeying Eq. (3.18), but eventually reduces to $\sqrt{t}$ as the central peaked region of the field expands.

The diffusing-growing nature of the field can be utilized as a method to convert the plasma oscillation into an electromagnetic wave in free space. As the growing field eventually hits the plasma-vacuum boundary through diffusion, radiation will be emitted into free space with temporally increasing amplitude. Indeed, such a field growth driven by this diffusion mechanism is the major advantage of our scheme in producing strong THz emission. To confirm this scenario of THz radiation, we have performed one- and two-dimensional particle-in-cell (PIC) simulations. A trapezoidal shape has been chosen for the plasma density profile, where the densities of the flat part are $1.25 \times 10^{18} cm^{-3}$ and $5.0 \times 10^{18} cm^{-3}$ (10 and 20 THz, respectively). To reduce any mismatch of radiation impedance, a density ramp-up over $100\mu\mathrm{m}$ is added to the flat plasma. Another important effect of the density gradient is that the field growth indicated by Eq. (3.18) is sustained for a longer time, eventually leading to stronger THz emission. The two counter-pulses are arranged so that they collide at $25\mu\mathrm{m}$ or $50\mu\mathrm{m}$ from the knee of the density gradient. The wavelength of one of the pulses is $870\mathrm{nm}$, which is typical for Ti:sapphire lasers and the other is detuned so that their beat resonantly drives the plasma oscillation. In the two-dimensional simulation, the pulses focus at the colliding point with $50\mu\mathrm{m}$ spot radius. The normalized vector potential of the pulse is 0.05, for which $I \sim 5 \times 10^{15}\ W/cm^2$ and $P \sim 0.2\ TW$.

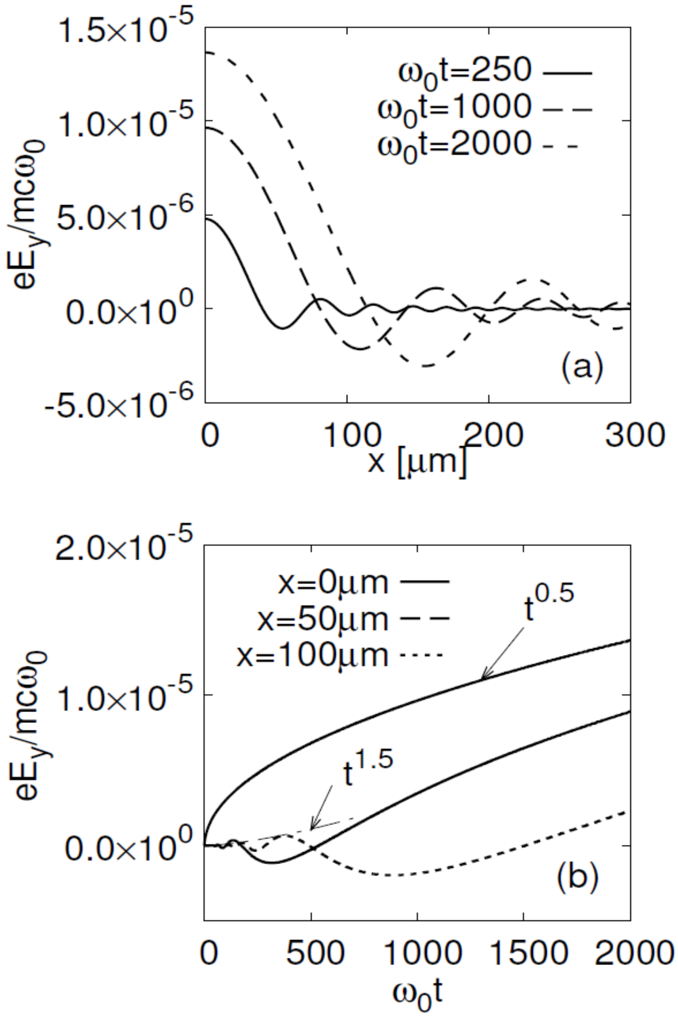

Figure 3.2 : (a) Spatial profile of the diffusing field at different times and (b) its temporal growth at different positions.

Fig. 3.3 (a) is an image of the THz emission obtained from two-dimensional PIC simulations. The diffusion and growth of the field measured on the axis [Fig. 3.3 (b)] takes on a very similar shape to the theoretical model. To observe the long time behavior of the signals, several one-dimensional PIC simulations have also been performed with the same parameters, varying the distance from the plasma edge to the pulse collision point as shown in Fig. 3.3 (c). In this figure, THz emission grows as $\mathrm{t}^{3/2}$ initially, but soon evolves into $\sqrt{t}$ dependence, which is exactly the same feature as shown in Fig. 3.2 (b). When the pulse collision occurs further into the plasma, it takes longer for the emission to grow, but eventually it reaches a comparable level (red and blue). Note that, due to the density gradient, a strong, but short duration emission by linear mode conversion [29] emerges simultaneously in the early stage. Though not fully plotted in the figure, the emission usually lasts up to an order of hundred pico-seconds, which produces quite a monochromatic frequency spectrum as shown in Fig. 3.3 (d).

3. Scaling of the THz amplitude

To obtain a scaling law for the field strength of the THz emission as a function of the driving pulse amplitude, I calculated the radiation current source, *i.e.* the $\hat{J}_0$ term in Eq. (3.2). Since the current is driven by the beat of two counter-propagating pulses, the electron oscillation is spatially fast-varying, where a linear portion of the oscillation is averaged out. However, the remaining smooth, nonlinear component can still be strong [45], forming a bunched longitudinal current oscillating at the plasma frequency. Once this averaged longitudinal current is generated, it induces a transverse current oscillation via the external magnetic field.

When the right- and left-going laser pulses are represented by

$$\begin{aligned} a_+ &= \hat{a}_+ e^{ik_+x - i\omega_+t}, \\ a_- &= \hat{a}_- e^{-ik_-x - i\omega_-t} \end{aligned} \tag{3.25}$$

, respectively, their beat is proportional to $e^{i(k_+ + k_-)x - i(\omega_+ - \omega_-)t} = e^{i(k_+ + k_-)x - i\Delta\omega t}$. Thus, it exerts the ponderomotive force on the electrons, in the same way, to yield the density perturbation

$$n_1 = \frac{1}{2}\left(\hat{n}_1 e^{i(k_+ + k_-)x - i\Delta\omega t} + c.c.\right) \tag{3.26}$$

Because the spatial average of n_1 disappears, the linear current $-\mathrm{e}n_0v_1$ does not contribute significantly to the electromagnetic radiation. However, a non-vanishing second-order current remains given by

$$\langle J_2 \rangle = -\frac{e}{4}\left(\hat{n}_1\hat{v}_1{}^* + \hat{n}_1{}^*\hat{v}_1\right) = -\frac{e\omega_p}{8kn_0}|n_1|^2 \tag{3.27}$$

And here, we have used the linearized continuity relation between $\hat{n}_1$ and $\hat{v}_1$

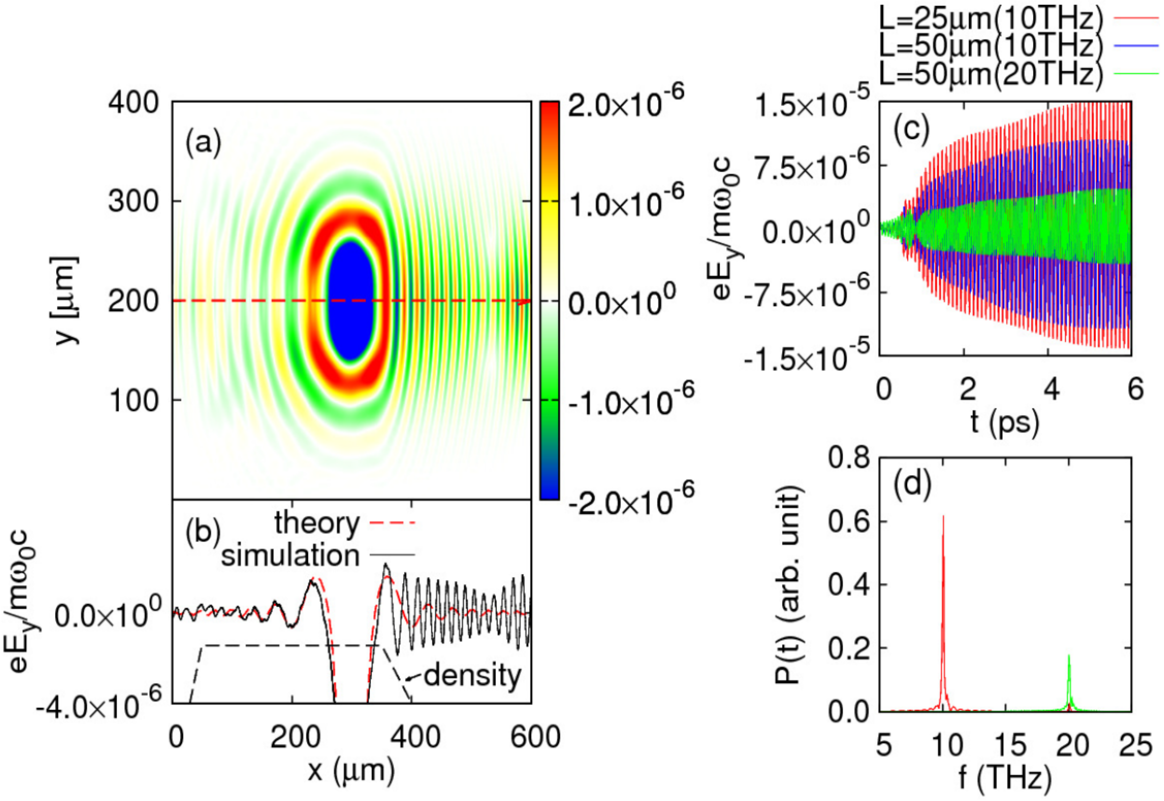

Figure 3.3 : (a) Diffusion of the transverse electromagnetic field inside a magnetized plasma (B = 2T) and THz radiation with $n_0 = 5.0 \times 10^{18} cm^{-3}$, a_0=0:05, and $\sigma =$ 4μm. The snapshot was captured at 1.3 ps after the pulse collision. (b) The field measured on the axis. (c) Temporal growth and saturation of the THz field for different collision points (L), and (d) the corresponding power spectra, with $n_0 = 1.25 \times 10^{18} cm^{-3}$, $\sigma =$ 4μm (red, blue) and $5.0 \times 10^{18} cm^{-3}$, $\sigma =$ 4μm (green).

$$\hat{v}_1 = \frac{\Delta\omega}{2kn_0}\hat{n}_1 \tag{3.28}$$

and assumed resonant driving, i.e. $\Delta\omega \cong \omega_p$. This spatially smooth nonlinear current, together with a linear self-current, drives the longitudinal electric field oscillations via the relation of

$$\frac{\partial \mathrm{E}_{x,smooth}}{\partial \mathrm{t}} = -4\pi\left(J_{1,self} + \langle J_2\rangle\right). \tag{3.29}$$

After applying time derivative to both sides of Eq. (3.29), it is obtained the wave equation as follows

$$\begin{aligned}\left(\frac{\partial^2}{\partial t^2} + {\omega_p}^2\right)\mathrm{E}_{x,smooth} &= -4\pi\frac{\partial}{\partial t}\langle J_2\rangle \\ &= \frac{\pi e\omega_p}{2kn_0}\frac{\partial}{\partial t}|\hat{n}_1|^2\end{aligned} \tag{3.30}$$

Note that $k_+ \cong k_- = k$, so $k_+ + k_- = 2k$. To obtain the solution of Eq. (3.30) we evaluate the temporal evolution of $\hat{n}_1$ driven by the beat of the counter pulses. The process of the temporal evolution of $\hat{n}_1$ follows:

From the equation of motion excepting magnetic force term with the reason of weakly magnetized plasma, *i.e.* $\omega_c = eB_0/m \ll \omega_p$

$$\begin{aligned}\frac{\partial \mathrm{v}_1}{\partial \mathrm{t}} &= -\frac{e}{m}\mathrm{E}_1 + \frac{F_p(ponderomovive\,force)}{m} = -\frac{e}{m}\mathrm{E}_1 + \frac{c^2}{4}\frac{\partial|a|^2}{\partial x} \\ &= -\frac{e}{m}\mathrm{E}_1 - c^2k[Re\{ia_+{a_-}^*\}]\end{aligned} \tag{3.31}$$

and Poisson's equation

$$\frac{\partial \mathrm{E}_1}{\partial \mathrm{x}} = -4\pi e n_1, \tag{3.32}$$

resultant another form of wave equation can be derived as

$$\left(\frac{\partial^2}{\partial t^2} + {\omega_p}^2\right)\mathrm{E}_1 = -4\pi e n_0 c^2 k\frac{\partial}{\partial x}[Re\{ia_+{a_-}^*\}]. \tag{3.33}$$

Using Eq. (3.32), the amplitude part $\hat{n}_1$ corresponding to the terms of $\mathrm{e}^{\mathrm{i}(2kx-\Delta\omega\mathrm{t})}$ is expressed as

$$\frac{\partial\hat{n}_1}{\partial \mathrm{t}} = -i\frac{n_0c^2k^2}{\omega_p}a_+{a_-}^*, \tag{3.34}$$

where the terms of second times derivatives to $\hat{n}_1$ are neglected. For laser pulses assumed to be longitudinally Gaussian with the same amplitude a_0 and pulse duration τ, the pulse amplitude can be written as

$$\hat{a}_{\pm} = a_0 exp\left[-\frac{\left(t \mp \frac{x \pm L}{c}\right)^2}{\tau^2}\right]. \tag{3.35}$$

Note that it is arranged for the peaks of the pulses to overlap at $x = 0$ after propagation by distance L. Then, applying the Green function method

$$\left(\frac{d^2}{dt^2} + {\omega_p}^2\right)\mathrm{G}(t,t') = \delta(t - t') \ \ \Rightarrow \mathrm{G}(t,t') = \frac{e^{i\omega_p|t-t'|}}{2i\omega_p} \tag{3.36}$$

to Eq. (3.30), we obtain

$$\begin{aligned} E_{x,smooth} &= \frac{A(x)\tau^2\sqrt{\pi}}{i4\omega_p}\int_{-\infty}^{\infty} d\alpha e^{i\omega_p\left|t-\frac{\alpha\tau}{\sqrt{2}}+\frac{L}{c}\right|}\Phi(\alpha) \\ &= \frac{A(x)\tau^2\sqrt{\pi}}{i4\omega_p}\left[\left(\int_{-\infty}^{\frac{\sqrt{2}}{\tau}(t-L/c)} d\alpha + \int_{\frac{\sqrt{2}}{\tau}(t-L/c)}^{\infty} d\alpha\right) e^{i\omega_p\left|t-\left(\frac{\alpha\tau}{\sqrt{2}}+\frac{L}{c}\right)\right|}\Phi(\alpha)\right] \end{aligned} \tag{3.37}$$

,where $\alpha \equiv \frac{\sqrt{2}}{\tau}(t' - L/c)$,

$$\Phi(\alpha) \equiv \frac{e^{-\alpha^2}}{\sqrt{\pi}}\int_{-\infty}^{\alpha} dx e^{-x^2} \tag{3.38}$$

and

$$A(x) \equiv \frac{2\pi e n_0 c^4 k^3}{\omega_p} {\hat{a}_{0+}}^2 {\hat{a}_{0-}}^2 \mathrm{e}^{-4x^2/\tau^2 c^2} \tag{3.39}$$

By fitting using error function $\Phi(\alpha)$ can be approximated as

$$\Phi(\alpha) \approx \mathrm{B} e^{-(\alpha - x_0)^2/b^2} \tag{3.40}$$

,where $\mathrm{B} = 0.61, x_0 = 0.36$ and $b = 0.82$. If t is sufficiently large enough, second term of Eq. (3.37) is neglected, then Eq. (3.37) is reduced to a finally approximated form

$$E_{x,smooth} = \frac{A(x)\tau^2\sqrt{\pi}B}{i4\omega_p} e^{i\omega_p t}\int_{-\infty}^{\infty} d\alpha e^{-(\alpha - x_0)^2/b^2} e^{-i\omega_p\left(\frac{\alpha\tau}{\sqrt{2}}+\frac{L}{c}\right)}. \tag{3.41}$$

Then finally the spatially averaged longitudinal oscillation amplitude becomes

$$\frac{eE_{x,smooth}}{m\omega_0 c} = \frac{\pi}{16}\sigma^2 k^2 {\hat{a}_{0+}}^2 {\hat{a}_{0-}}^2 \mathrm{e}^{-4x^2/\sigma^2} e^{-0.08405{\omega_p}^2\tau^2} sin\left(\omega_p t - \frac{\omega_p \tau x_0}{\sqrt{2}}\right) \tag{3.42}$$

,where ω_0 is the laser's angular frequency. An interesting feature of this equation is that the longitudinal field depends only weakly on the plasma density via the exponential term, which is quite a different feature from the single-pulse-driven wake field.

By applying an external magnetic field in the transverse direction, the longitudinal electric field given by Eq. (3.42) can be partially converted to the transverse field oscillating with the same frequency ω_p. Here the ratio of the transverse oscillation to the longitudinal one is given by

$$E_y = \frac{\omega_c}{\omega_p} E_{x,smooth} \tag{3.43}$$

, which yields

$$\frac{eE_y}{m\omega_0 c} \cong \frac{\pi}{16}\frac{\omega_c}{\omega_p}\sigma^2 k^2 {a_0}^4 e^{-0.08405{\omega_p}^2\tau^2} \tag{3.44}$$

, where the assumption is $\hat{a}_{0+} = \hat{a}_{0-} = a_0$. Then the radiation source current is calculated from the relation

$$-4\pi J_y = \frac{\partial \mathrm{E}_y}{\partial \mathrm{t}} \tag{3.45}$$

When the plasma-vacuum boundary is sharp, and the pulse collision point is located exactly at the edge of the plasma, the transverse field given by Eq. (3.44) is coupled to the vacuum without experiencing the diffusion and growth. Thus Eq. (3.44) gives the scaling of the minimum THz amplitude as a function of the driving pulse amplitude. An interesting point in this scaling is that the THz amplitude is proportional to ${a_0}^4$, corresponding to P^2, where P is the power of the driving laser pulse. This is significantly different from the single-pulse driven systems, where the emission amplitude is proportional just to P. From this different scaling, and due to the k^2factor, one of which is replaced by a much smaller value σ^{-1} in the single-pulse case, we expect the counter-propagating pulse scheme to generate a much stronger THz wave than the single-pulse driven schemes, even with very moderate laser power. More detailed comparison between Eq. (3.44) and the single-pulse scaling shows that the counter-pulse effect dominates the single-pulse effect, when $\mathrm{a}_0 > \mathrm{a}_{th}$, where

$$\mathrm{a}_{th} \sim 0.42\frac{1}{\sqrt{N}}\frac{\omega_p}{\omega_0} \tag{3.46}$$

and the single-pulse scaling is

$$\frac{eE_{x,single}}{m\omega_0 c} \cong \frac{\sqrt{\pi}}{8}{a_0}^2\frac{\omega_p\omega_c}{\omega_0}\tau e^{-{\omega_p}^2\tau^2/4}. \tag{3.47}$$

Here N represents the number of oscillations of the laser field within the pulse duration, usually > 10, and $\omega_p/\omega_0 \ll 1$, thus this condition is satisfied even for a small a_0.

Fig. 3.4 shows the theoretical curves of the THz amplitude from those two different schemes for $n_0 = 5 \times 10^{18}\ cm^{-3}$ and $n_0 = 1.25 \times 10^{18}\ cm^{-3}$, corresponding to 20 and 10 THz, respectively. In Fig. 3.4, the simulation data (circles) exhibits saturation, which arises from wave-breaking of the

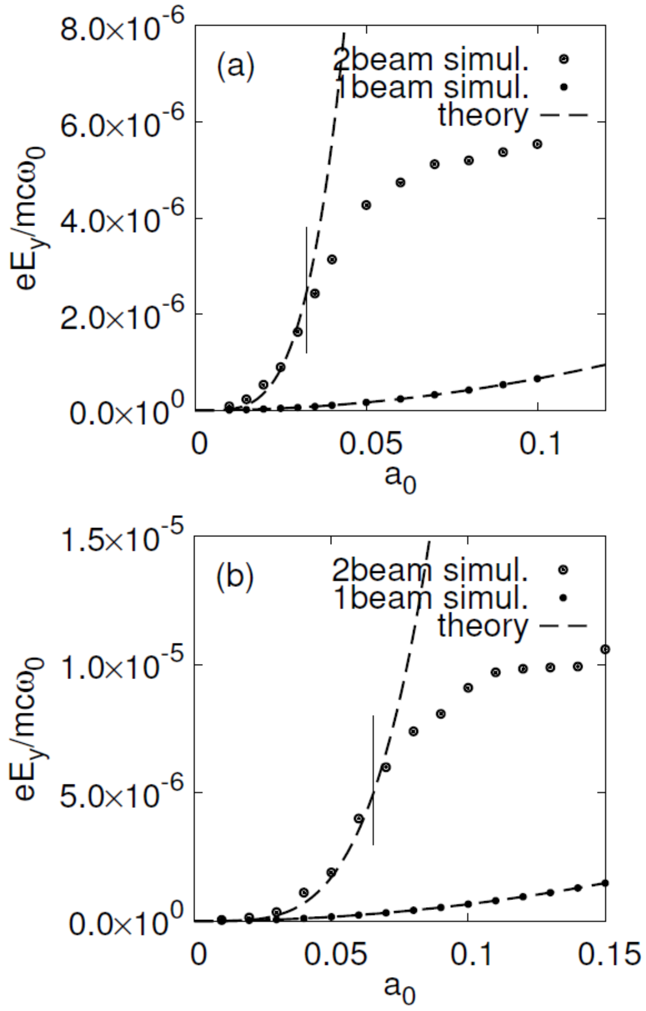

Figure 3.4 : Amplitude of the terahertz emission as a function of a0 for the counter-propagating pulse scheme and the single-pulse scheme with magnetic field B = 2T. (a) The case for $n_0 = 5.0 \times 10^{18} cm^{-3}$ (20 THz) and $\sigma =$ 4μm. (b) The case for $n_0 = 1.25 \times 10^{18} cm^{-3}$ (10 THz) and $\sigma =$ 8μm. The vertical bars represent the theoretical wave-breaking points from Eq. (3.51)

spatially fast varying wave. One major effect of wave-breaking is the suppression of the plasma current by kinetic detuning [46]. From the fact that it occurs when the electron fluid velocity, which is

$$\hat{v}_1 \cong \sqrt{\frac{\pi}{8}}\, {a_0}^2 \,\frac{\omega_0 \sigma}{2} \tag{3.48}$$

from the linearized continuity equation, exceeds the phase velocity of the plasma wave

$$\hat{v}_{ph} = \frac{\omega_p}{2k} \tag{3.49}$$

, we estimated the laser amplitude for saturation to be

$$a_{sat} = \left(\frac{8}{\pi}\right)^{1/4} \sqrt{\frac{\omega_p}{\omega_0 \sigma k}}. \tag{3.50}$$

In addition, the scaling for very low a_0 obeys ${a_0}^2$ rather than ${a_0}^4$, though not as apparent in the figure, when $a_0 < a_{th}$. As a consequence, operating with a_0 between a_{th} and a_{th} may yield optimum energy conversion from laser to THz emission.

As mentioned above in Fig. 3.3 (b), the density gradient helps the diffusing field to grow and to yield much stronger THz emission than for the sharp boundary case. Such a feature is verified by the PIC simulations, as shown in Fig. 3.5, where a significant enhancement due to the density gradient is apparent. Indeed, the positive effect of the density gradient is one of the advantages of the field diffusion mechanism. Because the every realistic plasma from a gas-jet or capillary discharge used for laser-plasma interactions has a natural density ramp-up, the experimental conditions can be greatly relaxed in our diffusion-growth scheme. Furthermore, even though a varying density is employed, the radiation frequency is not influenced much by that since our scheme is based on the local oscillation of the plasma. Note that, for a density gradient, the THz frequency is usually chirped leading to broad-band emission when driven by a single pulse.

4. Conclusion

In summary, we have proposed and investigated a novel method for obtaining strong THz emission based on a driven-diffusion mechanism. We obtain, analytically, the temporal growth of the diffusing electromagnetic field by solving the constantly driven complex diffusion equation. For the driving term of the diffusing field, a long lasting, localized current source for the radiation can be evoked by two counter-propagating laser pulses colliding in the weakly magnetized plasma. From analytic theory, we found that the THz amplitude scales with P^2 of the driving pulse, which is verified by one-dimensional PIC simulations. This scaling gives much stronger emission than for

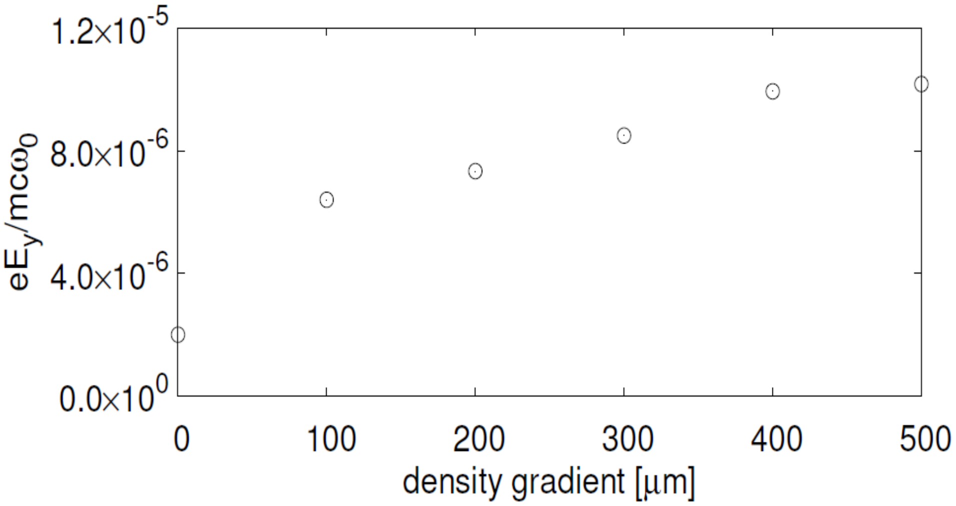

Figure 3.5 : Dependence of the amplitude of THz emission on the length of the density gradient for $n_0 = 1.25 \times 10^{18} cm^{-3}$ (10 THz), $a_0 = 0.05$, $\sigma = 8$μm, and B = 2T.

single-pulse-driven systems, which is proportional just to P. Such significant enhancement of the THz amplitude arises from two factors: one is the stronger ponderomotive force produced by counter-propagating pulses compared with a single pulse for a given total energy of the pulses. The other is the growth of the emission by a driven-diffusion mechanism of the electromagnetic field.

Finally, we confirmed the feasibility of the proposed scheme for experimental realization by showing that it does not require any strict condition for the plasma or lasers such as the sharp plasma edge or the exact pulse collision point. Moreover, we discover that the density gradient positively enhances the emission amplitude. From such results, we note the experimental condition can be significantly relaxed. We suggest the following proof-of-principle experimental parameters: a couple of millimeter plasma with density of order $10^{18}\ cm^{-3}$ and density-ramp-up over 100μm, which is readily available from gas jet or capillary discharge. The intensity of the laser pulses used in our simulation is $5 \times 10^{15} W/cm^2$, which yields 50 MV/m of the THz amplitude. Therefore we expect a few TW pulses with 200μm spot radius may yield THz power of order 0.1MW.

Chapter 4

Measuring the magnetic field of a magnetized plasma using Raman scattering

1. Introduction

Raman Scattering in plasma is a prominent non-linear process in high power laser plasma interaction and is considered as an important diagnostic tool for various plasma applications such as plasma-based electron acceleration and inertial confinement fusion (ICF). These plasma-based applications are highly dependent on the status of plasma such as the homogeneity of plasma density, the temperature, and magnetic field. For example, both of the Raman forward scattering (RFS) and the Raman backward scattering (RBS) were used to measure the plasma density in under-dense plasmas [1, 47, 48]. It was also shown by particle-in-cell (PIC) simulations that the temperature and density of an homogeneous plasma are simultaneously detectable by measuring RBS and RFS together [2]. Meanwhile, one recent experimental result has shown that the spatial information of a plasma density is extractable using the Raman backward amplification technique based on stimulated Raman scattering [44]. Properties of laser propagation in magnetized plasmas have been also studied widely, where most of the works are focused on self-generated high magnetic field or Cerenkov wake radiation [36, 38, 49, 50]. Theoretical works for the case of X-mode [51, 52] showed that RBS spectroscopic peak shifts from the incident laser's frequency by an amount of upper hybrid frequency ω_h and the scattering growth rate decreases as the magnetic field increases. However, there has been almost no experimental or simulation study on the effects of external magnetic field on RBS and RFS. The reason may be partially that in the regime of short-wavelength laser pulse $(\lambda{\sim}1\mu m)$, a huge magnetic field reaching a few hundred Tesla is required to clearly see its effects. Fortunately, the development of highly intense lasers with tens-of-micrometer-wavelength like a maser can give a more chance of studying experimentally the Raman scattering in magnetized plasma; for instance, terawatt-level and 5-ps pulse of $10\ \mu\text{m}$ CO2 lasers are now available [53].

In a previous publication by one of the authors of this chapter, they proposed a method to measure the plasma density and temperature simultaneously utilizing the different sensitivities of the RBS and RFS to the plasma temperature [2]. Specifically, the thermal frequency shift of the Bohm-Gross wave, ${v_{th}}^2k^2$, depends on the wave number, so the RBS, which has a large wave number, is influenced more significantly by the plasma temperature than the RFS which has only a small wave number. By detecting and comparing the RFS and RBS frequency shifts simultaneously, the plasma density and temperature information can be extracted together.

In this chapter, it is suggested another method to measure simultaneously the time- and space-averaged magnetic field as well as the plasma density utilizing the different behaviors of the RBS and RFS in a magnetized plasma.

2. **Theory**

When a pump laser pulse is irradiated onto magnetized plasma, it can be Raman-scattered into another electromagnetic waves and plasma waves. Theoretically, the plasma wave in such an environment is not purely electrostatic, but it contains an electromagnetic component. So the three waves, i.e., the pump, scattered, and the plasma waves, follow the X-mode dispersion relation as follows [7]:

$$\frac{c^2k^2}{\omega^2} = \frac{c^2}{{v_\varphi}^2} = \frac{1}{{\beta_\varphi}^2} = 1 - \frac{{\omega_p}^2}{\omega^2}\frac{\omega^2 - {\omega_p}^2}{\omega^2 - {\omega_h}^2} \tag{4.1}$$

, where v_φ is the phase velocity. Note that we assumed the relativistic effect can be neglected and the ions are stationary in the time scale of the scattering. In this scattering process, RFS yields two sidebands: one is the upshifted, and the other is the downshifted by an amount of plasma wave frequency. On the other hand, RBS yields only a downshifted sideband [54]. Usually, such a scattering occurs with a maximum growth rate, when the three waves, i.e., the pump (ω_0, k_0), scattered (ω_s, k_s), and the plasma (ω, k) waves, satisfy the resonance condition. When the forward-scattering is relevant, the resonance condition between the three waves is

$$k_0 = k_f + k_{fs}, \qquad \omega_0 = \omega_f + \omega_{fs} \tag{4.2}$$

Here, the subscripts s and f represent the “scattered” and “forward,” respectively. For this case, the phase velocity of the plasma wave is fast, i.e.,

$$\beta_{\varphi,f} = \frac{1}{c}\frac{d\omega_f}{dk_f} \cong \frac{1}{c}\frac{|\omega_0 - \omega_{fs}|}{|k_0 - k_{fs}|} \approx 1 \tag{4.3}$$

, which is nothing but a group velocity of the high-frequency pump wave. On the contrary, the wave number of the plasma wave for an exactly backward scattering is roughly twice the pump’s wave number

$$k_b = k_0 + k_{bs} \cong 2k_0, \qquad \omega_b = \omega_0 - \omega_{bs} \tag{4.4}$$

Therefore, the RBS induces a slow plasma wave with

$$\beta_{\varphi,b} \approx \frac{1}{c}\frac{|\omega_0 - \omega_{bs}|}{2k_0} \ll 1. \qquad (4.5)$$

Note that all those resonance condition can be interpreted as results of energy and momentum conservation between the photons and plasmons.

As the phase velocities of the plasma waves involved in RFS and RBS are hugely different to each other, the spectral dependence of the scattered waves on the magnetic field shows a significantly different behavior. Such a point can be easily seen by representing the frequency of the plasma wave as a function of the phase velocity from Eq. (4.1) as follows:

$$\frac{\omega^2}{{\omega_p}^2} = \frac{1 + A + {\omega_c}^2/{\omega_p}^2}{2} + \sqrt{\left(\frac{1 + A + {\omega_c}^2/{\omega_p}^2}{2}\right)^2 - A} \qquad (4.6)$$

, where

$$\mathrm{A} \equiv \frac{1}{1 - 1/{\beta_\varphi}^2}. \qquad (4.7)$$

For the case of RFS, $\beta_{\varphi,f} \sim 1$, so the frequency of the plasma wave from Eq. (4.6) becomes, up to the first order of A^{-1}

$${\omega_f}^2 \cong {\omega_p}^2\left(1 - \frac{1}{A}\left(1 + \frac{{\omega_c}^2}{{\omega_p}^2}\right)\right). \qquad (4.8)$$

In Eq. (4.8), the magnetic field effect is only a small term because $|A| \gg 1$, so the forward plasma wave frequency is very close to the plasma frequency ω_p. Therefore we can expect the RFS frequency is not affected significantly by the external magnetic field. Especially when the driving pump pulse is short enough to leave a wake-field behind, it is called the Cerenkov wake [36]. In the case of RBS, however, $\beta_{\varphi,b} \ll 1$, so A in Eq. (4.7) approaches to zero yielding

$${\omega_b}^2 \cong {\omega_h}^2 = \sqrt{{\omega_c}^2 + {\omega_p}^2}. \qquad (4.9)$$

Then from Eq. (4.8) and (4.9), and the resonance conditions aforementioned, the plasma wave frequency can be represented as a function of the magnetic field both for RFS and RBS as in Fig. 4.1, where it is shown that the plasma wave frequency for the RBS case is more strongly influenced by the magnetic field than that for the RFS. As a consequence, it is expected that the RBS shows more frequency shift by the magnetic field effect than the RFS. Since there is almost no magnetic field information contained in RFS signal, it can be used as a reference to measure the plasma density. Then the magnetic field information can be extracted by measuring the additional frequency shift of RBS.

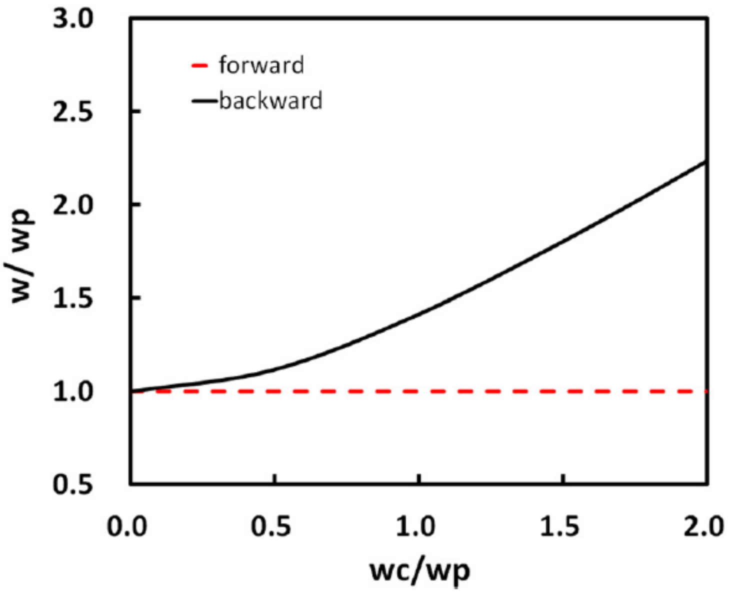

Figure 4.1 : Plasma wave frequency depending on magnetic field obtained from Eq. (4.8) and (4.9).

Experimentally, the intensity and direction of the magnetic field as well as the plasma density can probably be measured by irradiating the pump pulse in various different angles, and detecting simultaneously the for- and back-scattered signals.

3. **Simulation**

As a test of such an idea, we performed a series of one-dimensional PIC simulations of the Raman scattering in magnetized plasma. For separation of the backscattered and forward-scattered signals, we employed the directional field split method for the field solver [8]. In the simulations, the external magnetic field was perpendicular to the propagation of the pump laser pulse. Then a longitudinally Gaussian pump laser pulse with the wavelength $10\mu\mathrm{m}$ and pulse duration $\tau = 10\mathrm{ps}$ was launched. The peak value of the normalized vector potential of the pump pulse was $a_0 = eE_{0y}/m\omega_0 c = 0.3$. We also loaded a cold, magnetized plasma with densities $n_0 = 1.0 \times 10^{15} cm^{-3}$ and $1.0 \times 10^{17} cm^{-3}$, which corresponded to $\omega_p/\omega_c = 0.0095$ and 0.095, respectively. Here, we used a linearly polarized laser field in y direction. The plasma was magnetized by a z-directional various DC external magnetic fields. The laser pulse propagated to the right x-direction in the simulation window, so the right going and left-going fields contained the RFS and RBS signals, respectively.

Fig. 4.2 is the simulation result for the magnetic field 20Tesla measured at $t = 43.3\,ps$. Fig. 4.2 (a)–(c) show the right going field, the left going field, and the k-spectra of the RFS and RBS signals, respectively. In the case of RFS spectrum, only the lower sideband is presented for comparison with the downshifted RBS frequency. From Fig. 4.2 (c), it is clearly seen that the additional frequency shift by the magnetic field in RBS is large enough compared to the bandwidth of each peak, so it can be readily utilized to get the magnetic field strength. Note that the RFS signal is superposed by the original pump wave, so it is not distinguishable in the figure, while the backscattered signal can be separately observed as in Fig. 4.2 (b).

In Fig. 4.3, it is shown that the Raman peak shift for different magnetic fields measured from the simulations agree well with the theory. Because of the low growth rate of RFS in low plasma density, we could not detect the RFS in the case $n_0 = 1.0 \times 10^{15} cm^{-3}$. However in real experiments, the RFS signal might be detected more easily by using a longer pump pulse. In the case of higher plasma density of $n_0 = 1.0 \times 10^{17} cm^{-3}$, Fig. 4.3 (b) shows a good agreement between the theory and the simulations even in extremely high magnetic field. To get more confidence in the simulation results, we measured the growth rate of the backscattering and compared it with the theory. The previous theoretical study of RBS growth rate(γ) in a cold, magnetized plasma [51] shows

$$\gamma = \frac{1}{2} k_0 V_0 \sqrt{\frac{{\omega_p}^2}{\omega_0 \omega_h}} \tag{4.1015}$$

, where V_0 is the pump wave induced velocity of the electrons. When the external magnetic field is small *i.e.* $\omega_c \ll \omega_p$,

$$a_0 \cong \frac{V_0}{c}. \tag{4.11}$$

To compare the growth rates from Eq. (4.10) and simulations, we used the fact that the intensity of the scattered wave is proportional to $exp[\gamma_{eff}\tau_{eff}]$. Here, we approximated the Gaussian pulse durations and peak amplitude a_0 used in the simulations to the square shape with $\tau_{eff} = \tau/2$ and $a_{0\text{eff}} = a_0/\sqrt{\pi}$. Because Eq. (4.10) is valid for an infinitely long homogeneous laser pulse, the simulation results can directly compared to it only after such averaging and approximating the Gaussian shape to the square shape. It is shown in Fig. 4.4 that the ratio of the spectral peak intensity of the scattered wave to that for $\mathrm{B} = 0$ is matched well with the theoretical expectation.

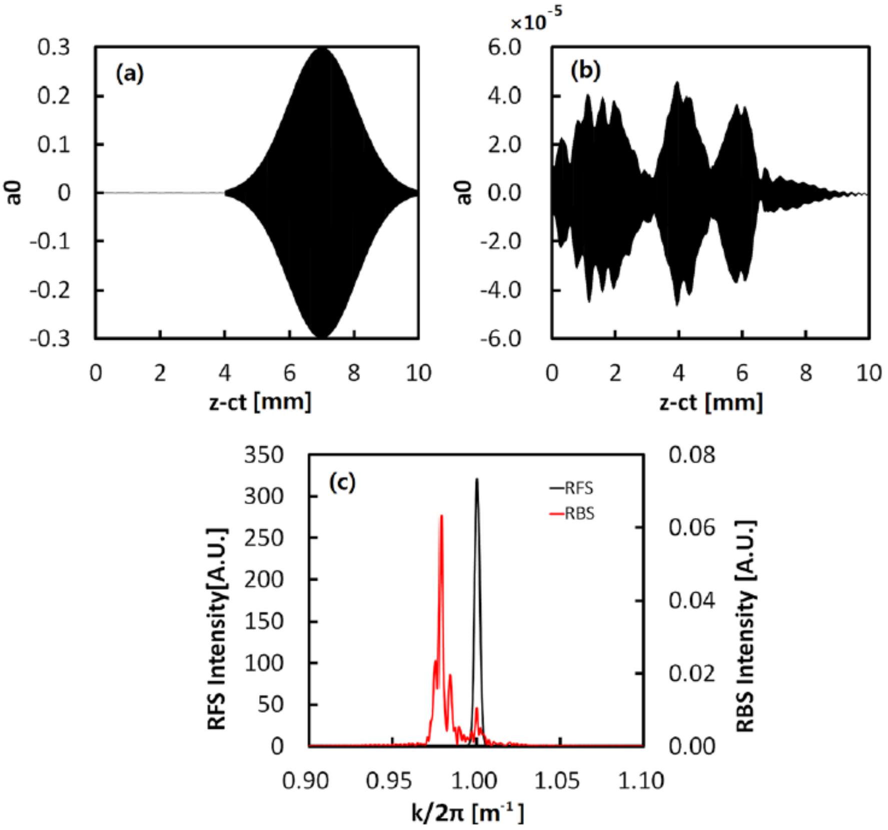

Figure 4.2 : Measured (a) right going field and (b) left going field at t = 43.3ps and for magnetic field B=20T using a directional field splitting method.
(c) The frequency spectra for RFS (black) and RBS (red) are also shown.

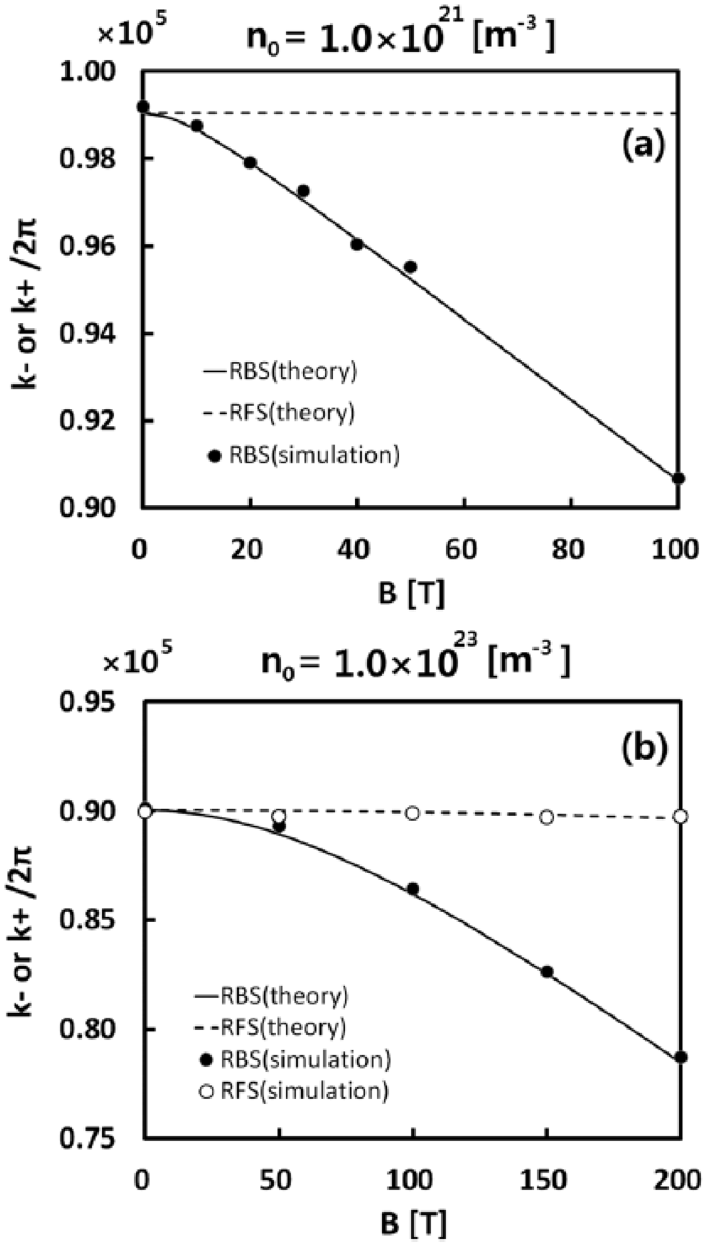

Figure 4.3 : Frequency shifts of RBS and RFS depending on the external magnetic field for (a) the plasma density $n_0 = 1.0 \times 10^{15} cm^{-3}$, where the RFS was too weak to be detectable in the given simulation range, and (b) $n_0 = 1.0 \times 10^{17} cm^{-3}$, where both RBS and RFS could be measured.

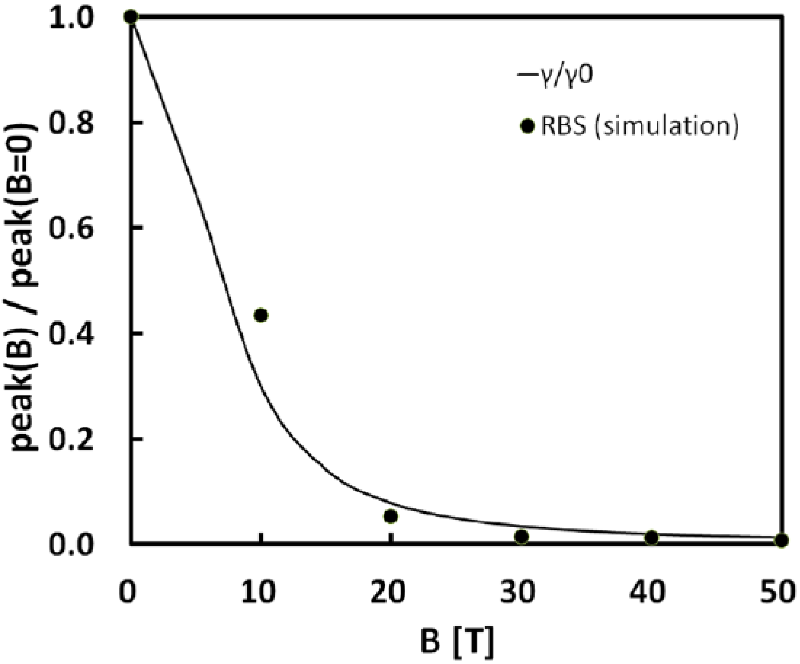

Figure 4.4 : The RBS peak intensity and the theoretical growth rate depending on the external magnetic field. The solid line indicates γ/γ_0 and the dot indicates measured peak intensity , where γ_0 is the growth rate for *B=0.*

4. Discussion and conclusion

Here, we discuss a potential experimental application of the suggested idea. The proposed diagnostic method, along with the previous one to measure the plasma temperature [2], can be realized in the experiments by simultaneously detecting RBS and RFS spectra of the pump laser pulse irradiated in various angles. Though the plasma diagnostics by Raman scattering is usually applied to a relatively high-density plasma above $10^{18} cm^{-3}$, we showed the suggested idea can also be used even in a low density plasma such as $10^{15} cm^{-3}$ or below. In that sense, one of the good applications of the proposed method might be the diagnostics of Tokamak plasma density and magnetic field, where the density is in the range of $10^{13} - 10^{15} cm^{-3}$ and the magnetic field at the core can reach up to a few or more than 10T depending on the operating regime. In that case the electron temperature

can be as high as $T \leq 10\ keV$ [55], so the currently proposed method probably should be combined with the previous method [2] of temperature measurement. To get a high enough growth rate in such a low density plasma, a longer duration of the laser pulse may be required. However, the pulse duration and focal spot are still very small compared to the length scale of the Tokamak plasma. Furthermore, the scattered signals may come dominantly from the focal spot of the pump pulse, where the laser intensity is the maximum. Since the spot size is also small compared to the plasma, any boundary effects can be neglected. So our method may provide a good way of pin-pointing the local plasma parameters. In that sense, though our method can be applied to homogeneous plasmas most effectively, such a limitation does not seem to diminish much the applicability of the suggested method. Note that when the dimensions of the plasma and the pump pulse are similar to each other, the plasma inhomogeneity may result in the bandwidth broadening of the scattered signals. On the other hand, the studies about the effects of density gradient on the growth of RBS can be found in Refs. [56, 57].

Before we summarize the works, it may be inspiring to compare the proposed idea with the Faraday rotation [58, 59], which is a well-known, robust method of measuring the magnetic field of a magnetized plasma. The rotation angle of the electric field polarization induced by the phase velocity difference of right-handed- and left-handed circularly polarized waves is described by

$$\Phi[rad] = 2.62 \times 10^{-17} \lambda^2 n_e B d, \ \ in\ cgs\ unit \tag{4.1216}$$

, where λ and d are the wave length and propagation distance of the pump pulse, respectively. Then, to obtain the rotation by 1° under the parameters of Fig. 4.3 (a), the pulse propagation length should be at least 3cm, which is larger than the Raman growth length by an order of magnitude: the RBS growth length is $\tau_{eff} \cong 5ps$, corresponding to 1.5mm.

In conclusion, it is proposed and studied a method to measure the density and the magnetic field of magnetized plasma utilizing the different frequency shifts of RFS and RBS for a given magnetic field. The idea was verified theoretically and also by one-dimensional PIC simulations. To clearly separate the back- and forward scattered signals, we employed the directional field splitting method for the field solver in the PIC simulations. We showed that the additional frequency shift of RBS by the magnetic field was large enough to distinguish the magnetic field effect. Furthermore, the growth rate of RBS measured from the simulations agreed well with theoretical predictions. And finally a potential experimental application regarding Tokamak plasma diagnostics was discussed.

Chapter 5

Electron trapping by a transversely ellipsoidal bubble in the laser wake-field acceleration

1. Introduction

Since Tajima and Dawson first suggested the concept of the plasma-based laser wake-field acceleration and calculated the efficiency of the acceleration comparing it to commercial acceleration methods [60], many people have investigated that field by theory, computer simulations, and experiments [61-68]. Recently, significant experimental results came out showing quasi-monoenergetic dense bunches of relativistic electrons with up to GeV-class energy [62, 63].

The generation of the accelerating wake-field comes from the ponderomotive force of the driving laser pulse. In this mechanism, electrons are first expelled by the ponderomotive force of the laser pulse and then are attracted back to their origins by the electric field induced by the charge separation. When the power of the driving laser pulse exceeds a certain threshold value, i.e., $\mathrm{P} > \mathrm{P}_c = 30[\mathrm{GW}] \times (\tau[\mathrm{fs}]/\lambda[\mu\mathrm{m}])^2$, this process forms a bubble, which is a spherically shaped electron-free region, having a sheath of higher electron density than that of the background in its rim. The bubble formed in this way propagates with the group velocity of the laser pulse so that

$$v_0/\mathrm{c} \simeq 1 - 1/2\gamma_0{}^2(\gamma_0 \simeq \omega_0/\omega_p) \tag{5.1}$$

, where $\omega_p = \sqrt{4\pi \mathrm{n}_0 \mathrm{e}^2/\mathrm{m}}$ is the electron plasma frequency, ω_p is the laser frequency and v_0, n_0, m, γ_0 are the laser group velocity, the background electron density, the electron mass, and the relativistic factor of the bubble, respectively.

Differently from conventional accelerators, in many experiments and simulations of the electron acceleration in the bubble regime, people do not use a separate beam injector, but instead the electrons are mostly self-injected into the bubble from the background plasma. Depending on the position and duration of such self-injection, most of the important beam parameters like the beam energy, energy spread, emittance, and beam charge are determined. Thus, understanding the self-injection mechanism is the key point in the laser plasma acceleration study. In other contexts, to make a large amount of electrons be self-injected, various additional techniques have been proposed such as two counter propagating laser pulses [64, 69], density transition [70, 71], ionization injection [72], etc.

From the numerical studies, it has been observed that electrons can be trapped by a large bubble with $R > 4$, where R is the normalized bubble radius to c/ω_p [61]. After that Kostyukov et al. derived the trapping condition for a spherical bubble, $\gamma_0 < R/\sqrt{2}$, where γ_0 is the gamma-factor of the bubble's backside [5]. As another mechanism of the electron trapping, it was theoretically suggested that the bubble deformation (usually the bubble's expansion) also traps electrons [6]. Moreover, it was shown in the same reference that subsequent bubble shrinking after the expansion makes a quasi-monoenergetic energy peak in the electron beam. Such a bubble expansion is actually dominant in longitudinal direction, so a longitudinally ellipsoidal bubble theory was introduced [73].

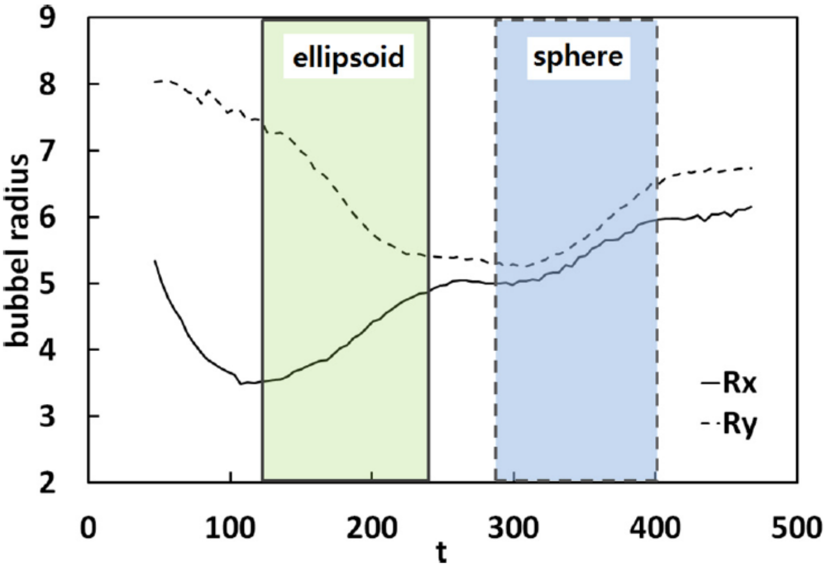

Figure 5.1 : Electron trapping as the bubble evolves temporally in its longitudinal (R_x) and transverse (R_y) sizes during an entire simulation. The solid box indicates the trapping region of an ellipsoidal shaped bubble, and the dashed box indicates that of a spherically shaped bubble. The previous spherical bubble model is not sufficient to explain the electron trapping in the ellipsoidal region.

In this chapter we describe the electron trapping condition in a transversely elongated ellipsoidal bubble, comparing it with the spherical one. As an overall feature, we show the evolution of the ellipsoidal bubble in Fig. 5.1, where we traced the longitudinal and transverse bubble size separately, and also the electron trapping by a three dimensional particle-in-cell (PIC) simulation. As can be seen from Fig. 5.1, the bubble starts with a transversely long ellipsoidal shape $R_y > R_x$ and then it slowly changes into a sphere ($R_y \cong R_x$). Here, the PIC simulation suggests that the trapping of electrons occurs not only in the spherical regime but also in the ellipsoidal regime, which is not explained by the previous spherical bubble model. To explain this, we generalized the bubble shape in the spherical bubble theory in Ref [5]. First, we introduce the relationship between the ratio of the longitudinal bubble size to the transverse one and the ratio of the longitudinal field slope inside the bubble to that in the transverse direction. By numerically integrating particle trajectories around such an ellipsoidal bubble potential, we obtained a modified trapping condition for an ellipsoidal bubble. Then, the newly obtained condition was verified by three-dimensional PIC simulations.

2. Model of the ellipsoidal bubble fields

The electromagnetic field in a bubble has a linearly increasing region around the center and a thin sheath region near the bubble's edge. Such a field shape is well approximated by the following function [3, 5]:

$$F(r) = k\frac{r}{4}\left(1 - tanh\frac{r-R}{d}\right) \tag{5.2}$$

,where R is the bubble radius, d the sheath thickness at the bubble boundary and k the scale factor of the field slope of the bubble. Then, the electromagnetic field inside the bubble becomes

$$\begin{aligned} E_x &= F(r) \\ E_y &= -H_z = \frac{F(r)}{2}. \end{aligned} \tag{5.3}$$

It is actually observed that Eq. (5.2) matches well the results from three-dimensional PIC simulations for a long enough simulation time. Integrating Eq. (5.2) with r, we obtain the bubble potential Φ as follows:

$$\begin{aligned} \Phi(r) = k\Bigg[\frac{r^2}{8} - \frac{1}{4}rd\, ln\left(\exp\left(\frac{r-R}{d}\right) + \exp\left(-\frac{r-R}{d}\right)\right) \\ + \frac{1}{4}d\int_0^r ln\left(\exp(\frac{r'-R}{d}) + \exp(-\frac{r'-R}{d})\right) dr'\Bigg]. \end{aligned} \tag{5.4}$$

Actually the bubble potential is defined as $\Phi = A_x - \phi$ using the gauge of $A_x = -\phi$, where A_x and ϕ are the *x* component of a vector potential and a scalar potential, respectively (see Sec. 3). By splitting the integration range at $r = R$, the final form of the potential for the region of $r \le R$ becomes

$$\Phi(r) = k\left[\frac{r^2}{4} - \frac{rd}{4} ln\left(1 + \exp\left(\frac{2(r-R)}{d}\right)\right) - \frac{d^2}{8} Li2\left(-\exp\left(\frac{2(r-R)}{d}\right)\right) + \frac{d^2}{8} Li2\left(-\exp\left(-\frac{2R}{d}\right)\right)\right] + \Phi_0 \tag{5.5}$$

and for the region of $r > R$

$$\Phi(r) = k\left[\frac{R^2}{4} + \frac{d^2\pi^2}{48} + \frac{d^2}{8} Li2\left(-\exp\left(-\frac{2R}{d}\right)\right) - \frac{rd}{4} ln\left(1 + \exp\left(-\frac{2(r-R)}{d}\right)\right) + \frac{d^2}{8} Li2\left(-\exp\left(-\frac{2(r-R)}{d}\right)\right)\right] + \Phi_0 \tag{5.6}$$

,where

$$Li_2(x) = \int_x^0 dt \frac{ln(1-t)}{t} \tag{5.7}$$

is di-logarithm function and

$$\Phi_0 = 1 - \frac{R^2}{4} \tag{5.8}$$

Is the potential at $r = 0$ to make the potential unity at $r = R$. When an ellipsoidal potential is assumed, we use different values for the radii in *x* and *y* directions in Eq. (5.6) , being marked by R_x and R_y. Then by assuming that the potential is constant around the bubble rim, we can set the potential as follows:

$$\Phi(R_x + 2d_x; k = k_x) = \Phi\left(R_y + 2d_y; k = k_y\right). \tag{5.9}$$

Here the multiplying factor of 2 in front of the sheath thickness *d* is just to ensure that the distance is far enough from *R*. We also use separate values for the field slopes in *x* and *y* directions, *i.e.*, k_x and k_y. Then from Eq. (5.6) and (5.9), we obtain the relationship between the field slopes and the bubble sizes in *x* and *y* directions as follows:

$$R_y = \sqrt{\frac{k_x}{k_y}} R_x, \tag{5.10}$$

$$d_y = \sqrt{\frac{k_x}{k_y}} d_x, \tag{5.11}$$

Eq. (5.10) tells us that the elongation of the ellipsoidal bubble is determined by the ratio of the bubble's field slope in each direction. This relation is well justified in Fig. 5.2, where it is shown that the measured values R_x, R_y, k_x and k_y from a three-dimensional PIC simulation satisfy well the theoretical relationship, Eq. (5.10) . Here, we notice that the scale factor k_x or k_y is obtained as the ratio of the slope of corresponding electric field component and the maximal value of the field slope

(1/2 for E_x and 1/4 for E_y, see Ref. [61]). Note that k_x and k_y do not exceed unity.

Eq. (5.5) and (5.10) along with appropriate $k(\theta)$ (see Eq. (14)) yield the following potential that, in turn, corresponds to elliptical shape of the bubble

$$\Phi = \frac{k_x}{4}x^2 + \frac{k_y}{4}y^2 + \Phi_0 \tag{5.12}$$

In Eq. (5.12), we neglected the screening terms that are important only near the bubble rim. Even though this result comes from phenomenological field slopes, the potential shape matched well the PIC simulation result as shown in Fig. 5.2 and 5.5.

3. Electron trapping in an ellipsoidal bubble

In this section, we describe the electron trapping condition under the general shape of the bubble described above, *i.e.*, $R_x \neq R_y$. When the group velocity of the driving laser pulse is close to the speed of light so that $\gamma_0{}^2 = 1/(1 - v_0{}^2/c^2) \gg 1$, the averaged electron motion in a slowly varying electromagnetic field is determined by the averaged Hamiltonian [74]

$$\mathrm{H} = \sqrt{1 + (1+P)^2 + \bar{a}^2} - v_0 P_x - \phi \tag{5.13}$$

, where P is the canonical momentum of the electron, $\bar{a}$ the vector potential of the laser field, and A and ϕ the slowly varying vector and scalar potentials, respectively. We change the variables from (x, P_x) to (ξ, P_ξ) using $\xi = x - v_0 t$ and $P_\xi = P_x$. The gauge is chosen as $A_x = -\phi$. Then, by defining the wake potential $\Phi = A_x - \phi$, the Hamiltonian equation of motion is given by [3]

$$\frac{dP_x}{dt} = -v_x\frac{\partial A_x}{\partial \xi} - v_y\frac{\partial A_y}{\partial \xi} + \frac{\partial \phi}{\partial \xi} = -\frac{1}{2}(v_x + 1)\frac{\partial \Phi}{\partial \xi} \tag{5.14}$$

$$\frac{dP_y}{dt} = -v_x\frac{\partial A_x}{\partial y} - v_y\frac{\partial A_y}{\partial y} + \frac{\partial \phi}{\partial y} = -\frac{1}{2}(v_x + 1)\frac{\partial \Phi}{\partial y} \tag{5.15}$$

$$\frac{d\xi}{dt} = \frac{p_x}{\gamma} - v_0 = v_x - v_0 \tag{5.16}$$

$$\frac{dy}{dt} = \frac{p_y}{\gamma} = v_y \tag{5.17}$$

where p is the kinematic momentum, and $\gamma = \sqrt{1 + p_x{}^2 + p_y{}^2}$. Here, we assume that A_y and $\bar{a}$ are negligible. To represent an ellipsoidal potential Φ for Eq. (5.14)–(5.17), we introduce angle dependence of *k* in Eq. (5.5) and (5.6) such that

$$k(\theta) = k_x cos^2\theta + k_y sin^2\theta, \tag{5.18}$$

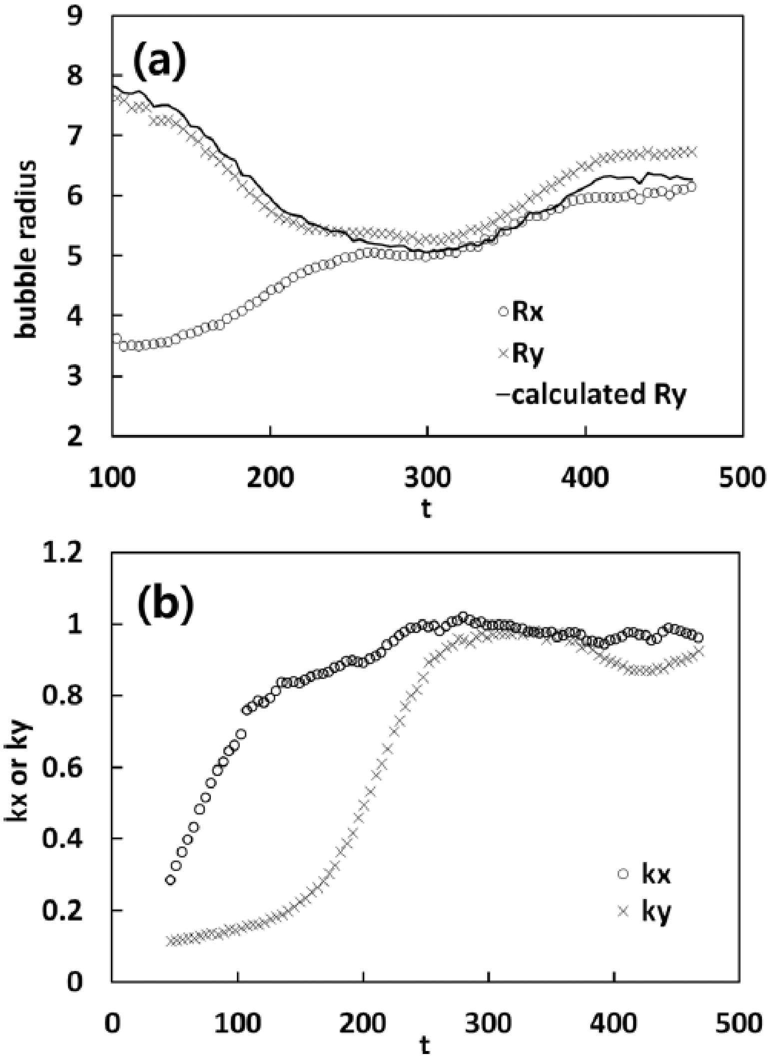

Figure 5.2 : Evolution of (a) the bubble sizes in longitudinal and transverse directions, and (b) the bubble field slopes in longitudinal and transverse directions. The “calculated R_y” is calculated from $R_x\sqrt{k_x/k_y}$. For this simulation, the laser pulse spot size is $r_L = 1.9k_p$.

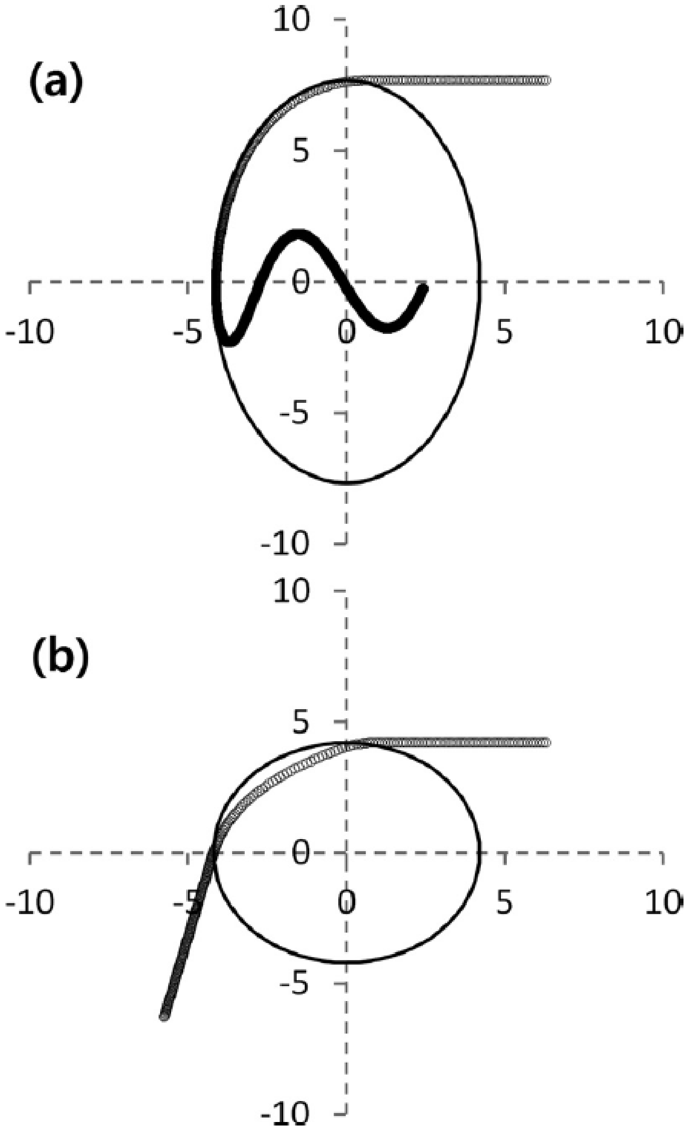

Figure 5.3 : Trajectories of electrons in (a) the ellipsoidal and (b) the spherical bubble potentials. The gamma factor of the bubble is $\gamma_0 = 4.5$, the bubble radius is $R_x = 4.2$, and the field slopes are (a) $k_x = 1$, $k_y = 0.3$, and (b) $k_x = k_y = 1.0$, for which the condition is non-trapping in the spherical bubble model.

, where θ is the angle measured from the *x*-axis. Then we numerically integrated Eq. (5.5), (5.6) and (5.14)–(5.17) to calculate the electron trajectories around the bubble potential to examine the trapping or non-trapping of electrons depending on the initial conditions of the bubble. Fig. 5.3 shows one example of such integration, where it is shown that an electron, which traces a non-trapping route around a spherical bubble, can actually be trapped if the bubble is elongated transversely for the same longitudinal bubble conditions such as the bubble speed and the longitudinal bubble size.

To obtain a trapping condition for the ellipsoidal bubble, we performed a series of trajectory calculations numerically, where we tried to determine the maximum value of γ_0 to trap the electron for a given k_y and R_x. Note that as γ_0 decreases, electrons can be trapped more easily. Those numerical results are shown in Fig. 4.4 for diverse values of k_y and R_x. Then finally the fitting of those numerical results yielded the following condition for electron trapping:

$$\gamma_0 \le \frac{R_x}{\sqrt{2k_y}} = \frac{R_y}{\sqrt{2}} \tag{5.19}$$

with parameters $k_x = 1$ and $d = 0.05$ (here we ignore *d*). Interestingly, the trapping condition is determined by just the transverse radius (R_y). When $R_x < R_y$, even though the focusing field becomes weaker than that of a spherical bubble, *i.e.*, $k_y < 1$, the electrons can still be trapped.

This result could be verified from the test potential calculation with more diverse k_y and R_y as shown in Table I. In this table, note that a k_x is fixed as unity, R_x decreases with decreasing k_y for a given R_y. Table 5.1 shows that the trapping condition does not change much as long as R_y is fixed though R_x changes, which is indicated in Eq. (5.19). This point provides us with an important insight regarding the trapping, since the transversely elongated ellipsoidal bubble appears quite often in the early stage of the bubble formation, which is the regime that the spherical theory does not explain the trapping.

Unfortunately we could not find more general relation of k_x, k_y and bubble radius except $k_x = 1$, so we confine the theory for the case of sufficiently large $k_x \sim 1$. However this is a good approximation, since usually the longitudinal field slope reaches the maximum value earlier than the transverse field.

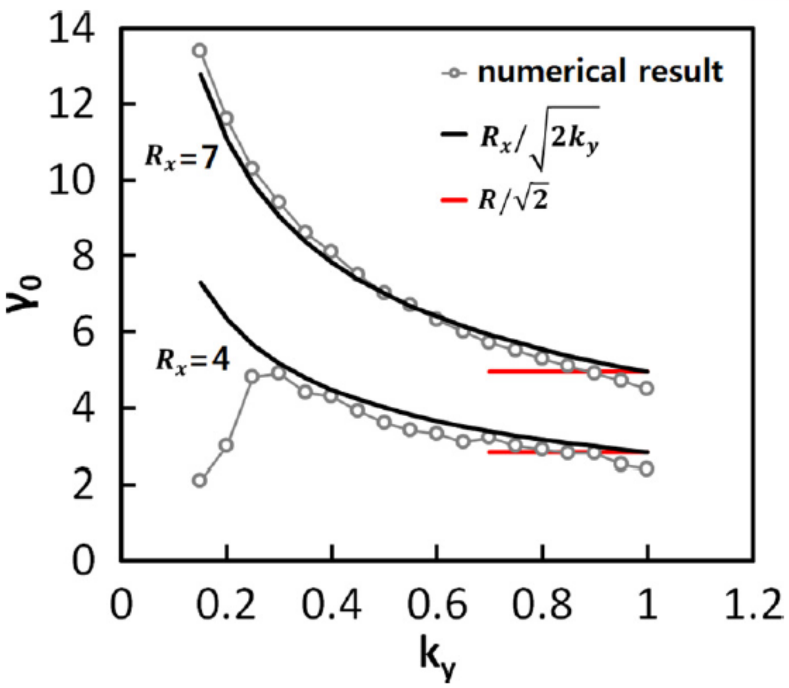

Figure 5.4 : The numerical calculation of the electron's trapping condition. The red solid line is the condition from the spherical model and the black solid line is a fitting curve with $R_x/\sqrt{2k_y}$ for $R_x = 4$ and $R_x = 7$. Other parameters are $d = 0.05$ and $k_x = 1$.

R_y	k_y							
	0.3	0.4	0.5	0.6	0.7	0.8	0.9	1.0
5.0	…	…	3.1	3.2	3.2	3.1	3.1	3.1
6.0	…	3.9	3.9	3.9	3.9	3.8	3.8	3.8
7.0	4.5	4.7	4.6	4.6	4.6	4.6	4.6	4.6
8.0	5.5	5.5	5.4	5.4	5.4	5.4	5.4	5.4
9.0	6.2	6.3	6.3	6.3	6.2	6.2	6.2	6.2

Table 5.1 : Maximum value of γ_0 obtained from the test potential calculations with fixed $k_x = 1$ and varying k_y and R_y.

4. Numerical simulation

We carried out three-dimensional PIC simulations to verify the theoretical result in Eq. (5.19). A detailed explanation and some benchmarks of the PIC code are described in Ref. [75]. To generate an ellipsoidal bubble, we used a pulse spot size larger than the plasma wavelength, $i.e. 1.9\lambda_p$. It is clearly observed in Fig. 5.5 that the bubble takes a transversely elongated shape in the early stage. Simulation parameters were as follows; the plasma density was $n_0 = 1.0 \times 10^{19} cm^{-3}$, the laser pulse was linearly polarized in the y direction with a Gaussian envelope, the wavelength was $\lambda = 0.8\,\mu m$, the normalized vector potential of the laser pulse was $a_0 = 3$, and the pulse duration was 26.6fs. The simulation stopped when the laser pulse passed the distance of 769λ inside the plasma.

As the pulse propagates through the plasma, the field slope of bubble starts to increase. When the spot size of the pulse is larger than the plasma wavelength, the transverse field slope is somewhat tardy in growth in comparison with the longitudinal field slope, because the edge field of the laser pulse makes it hard for the electrons to gather around the bubble's sides. In this way, the retarded growth of the transverse field slope forms a transversely elongated ellipsoidal bubble. However as the transverse field slope eventually catches up with the longitudinal field slope, the bubble deforms to the sphere and subsequently the longitudinally elongated bubble.

To compare the theoretical trapping condition Eq. (5.19) with the PIC simulations, the gamma factor γ_0 of the bubble should be calculated. For that purpose, we tracked all the individual particles for an entire simulation period. Trapped particles were initially positioned at the vertical (transverse) edge of a bubble with a low momentum, and they began to be trapped near the backside of the bubble. Then, the gamma factor of the backside of the bubble can be calculated by [5]

$$\gamma_0 \cong \sqrt{\frac{-1}{2dx/dx_0}} \tag{5.20}$$

,where *x* is the last position and x_0 the initial position of the trapped electrons in the trapping process. From the measured slope in x vs. x_0 graphs as in Fig. 5.6 (b) , and using Eq. (5.20), the gamma factor of the bubble's backside can be calculated, which is the grey solid line in Fig. 5.6 (d) . The dashed line in Fig. 5.6 (d) indicates the threshold value for the trapping in the spherical bubble model, *i.e.*, $R_x/\sqrt{2}$. If we follow $R_x/\sqrt{2}$, γ_0 is larger than this value during the time *t* from 100 through 250, so there should be no trapping according to the spherical model, while significant particle trapping was observed as in Fig. 5.6 (c) . However that range is actually the ellipsoidal regime, and γ_0 is located at the similar level of or below the modified threshold value $R_y/\sqrt{2}$, so the electron trapping in that temporal range is well explained by the ellipsoidal trapping condition. After the pulse passes through the non-trapping range around t = 260, the bubble took the spherical shape and satisfied both

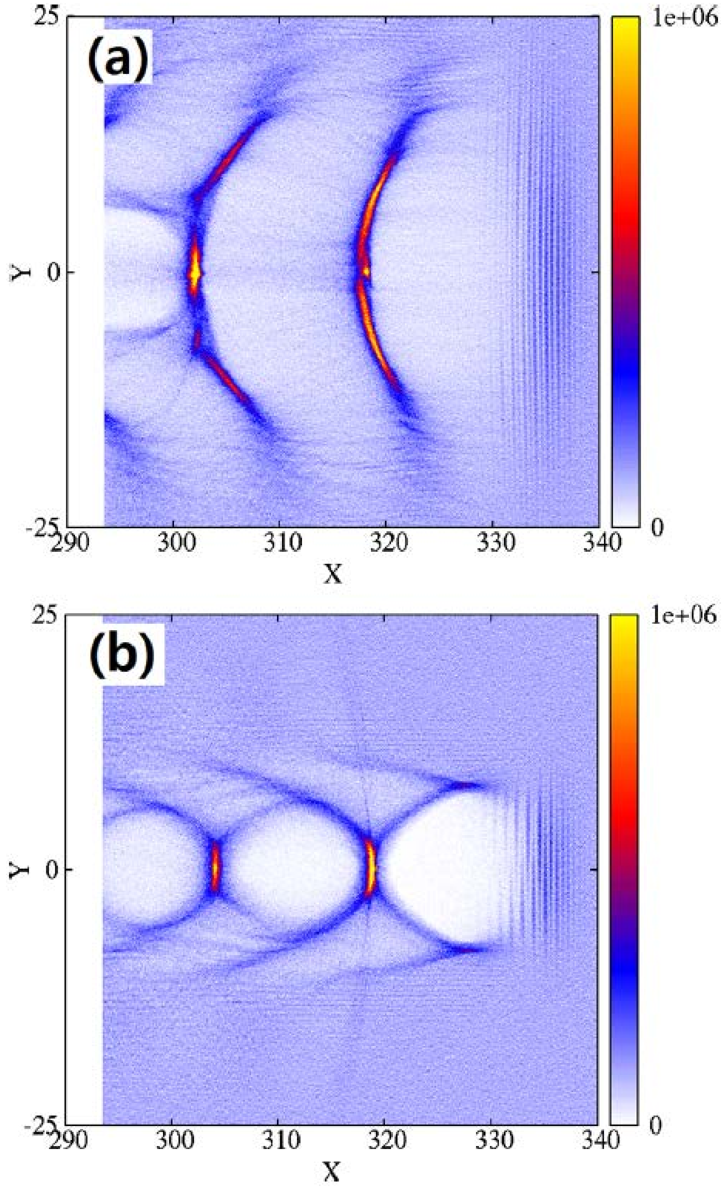

Figure 5.5 : The distribution of the electron density in the x–z plane from a three-dimensional PIC simulation. The measured laser pulse spot sizes are (a) $r_L = 1.9\lambda_p$, and (b) $r_L = 0.95\lambda_p$, when the laser pulse passes through 340λ in the plasma.

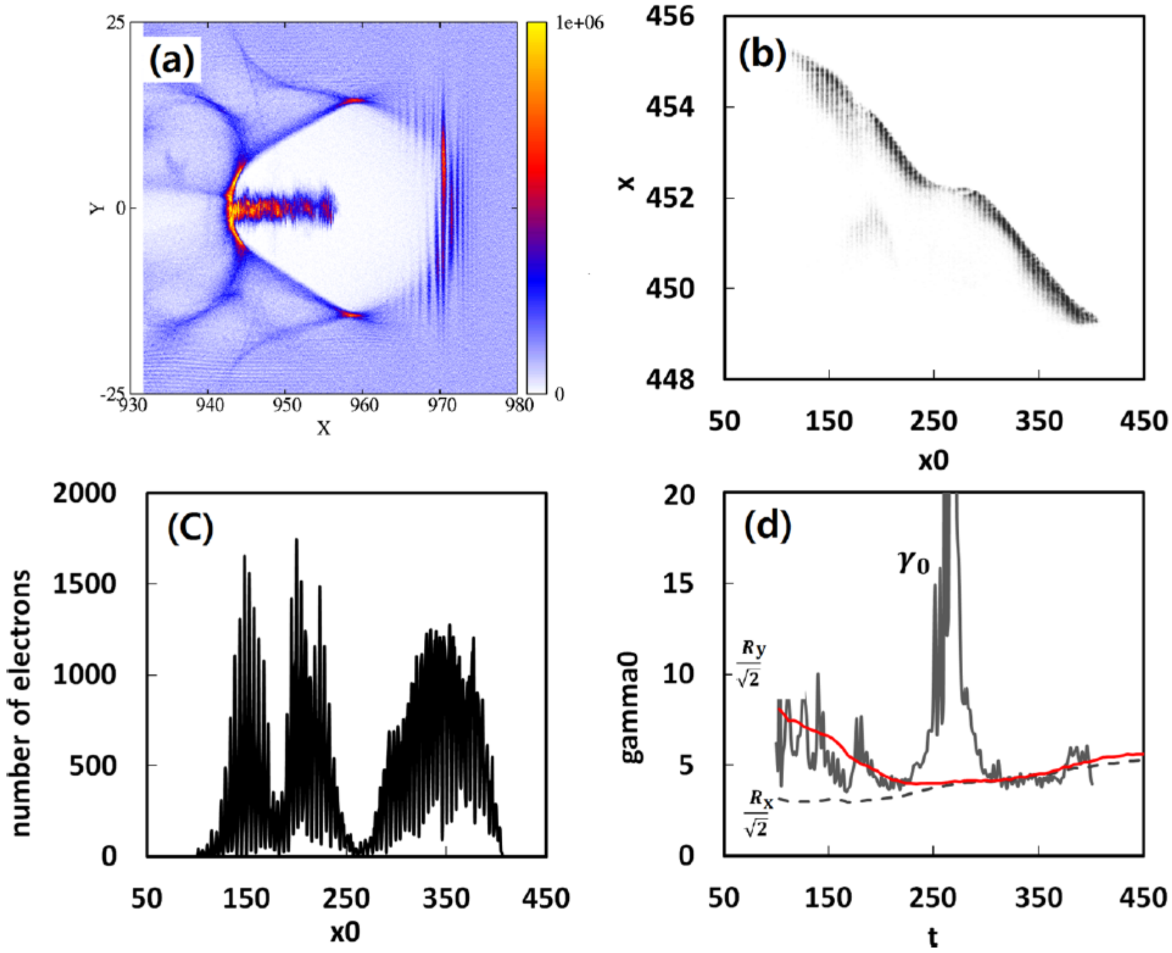

Figure 5.6 : (a) The distribution of the electron density in the x–z plane from a three-dimensional PIC simulation. (b) The last position x of trapped electrons as a function of x_0. (c) The number of trapped electrons scaled in an x_0 coordinate. (d) The gamma factor of the bubble's backside calculated from Eq. (5.20) and the measured slope of (b). The grey solid line is the gamma factor of the bubble's backside, the red solid line is $R_y/\sqrt{2}$, and the dashed line is $R_x/\sqrt{2}$ which is the same as the spherical model.

the original and the modified trapping conditions.

5. Conclusion

We have demonstrated by the theory and simulations the self-injection of electrons in the ellipsoidal bubble. Such a transversely elongated bubble appears commonly in the early stage of the pulse propagation, when the pulse spot size is larger than the plasma wavelength. Numerically we found a trapping condition for such ellipsoidal bubbles, where the trapping threshold of γ_0 is described more appropriately by $R_x/\sqrt{2k_y}$ instead of $R_x/\sqrt{2}$ and consequently is just described by $R_y/\sqrt{2}$. We have confirmed this result by numerical integration of test electron trajectories and full three-dimensional PIC simulations. Our result also implies that increasing the spot size of the driving laser pulse enhances early trapping of the electrons. However a more systematic study is required for the optimal bubble and pulse shapes, and the analytic origin of k_x and k_y relating the bubble density and Maxwell's equation, which are actually under progress.

Chapter 6

Summary and Future work

In this thesis the laser-plasma interaction is confined for the cold and electron only plasma. The theoretical models were studied and successfully verified from using PIC simulation for three applications of Terahertz generation, Raman scattering, and LWFA.

Through studying our new terahertz scheme theoretically, to the best of our knowledge, new physical phenomenon of diffusing and growing field have been first introduced by our group. Our scheme uses two lasers and an external magnetic field, so it is controllable to decide the current position and to make specific current shape like curved one. In a sense of user friendly application, this control parameter gives advantages of our scheme. If we can make curved current, the generated field may have a focusing effect. This multi-dimensional effect may give another aspect of applications which would be our future work. Even though we used an external magnetized field to make a diffusing and growing electromagnetic field, other new schemes would be possible for our new phenomenon. Because the current with cut-off frequency makes diffusing and growing fields, previously well-known terahertz schemes like 2 color laser scheme also have a chance to show diffusing and growing effects and it would be another future work.

We showed that Raman scattering can be a diagnostic tool for measuring external magnetic fields. We started with X-mode dispersion relation and derived that the plasma wave's phase velocity is a function of an external magnetic field. Though the forward scattering is non-sensitive to the magnetic field, it does not say that the forward scattering is not affected by the magnetic field. If the cyclotron frequency is big enough comparing the plasma frequency, the magnetic field effect starts to affect slightly. Although this thesis used Raman scattering for a diagnostic tool, the result of effectiveness of magnetic field gives an interesting consideration in LWFAs. Because the phase velocity of the plasma's wave is being small as the external magnetic field is getting stronger, the bubble's velocity has a lowered value than that of velocity in the case of non-magnetized plasma. As shown in Chapter 5, the bubble with a slow velocity has more chances to trap electrons, so the trapping effect of the magnetized plasma is also an interesting research. This thesis focused on 1D calculation, however, real situations have to be considered with multi-dimensional effects. Even though expanding to 2D and 3D calculation, the frequency shift of Raman scattering does not change. One considering point is the growth rate of scattering, which is a function of laser position and amplitude. Because the scattered wave's amplitude is sensitive to the laser's amplitude, a multi-dimensional effect like focusing is an interesting topic and is a subsequent study.

For LWFAs, the analysis for an ellipsoidal bubble potential was introduced. The theory was limited for a stationary potential, however, the 3D PIC simulation result says the bubble is changeable. For an accurate analysis, a non-stationary potential must be assumed. Nevertheless, as shown in our study, the bubble shape itself does affect the electron trapping. An ellipsoidal potential traps electrons at the initial stage than a spherical potential, so the large size of laser's spot may help increasing the number of accelerated electrons. We tested our result of relatively high plasma density for a real experimental situation. When the plasma density is low, it is hard to make an ellipsoidal bubble, because it needs really a high laser power for a big spot size. Although high energy of electrons needs the low plasma density, our result may still valuable for the other acceleration scheme like using multi plasmas of a high density plus a low density. The high density part of the plasma is used to make initial electron seeds, then these seed electrons are accelerated in the part of the low density plasma. So the ellipsoidal bubble is still useful for seeding electrons. Even though a real experiment is not easy to make an ellipsoidal bubble, it is curious as ever for the low density case. The bubble field enhances its strength as the laser passes through the plasmas, however, the rate of enhancement is low in a low plasma density and it is interesting to study the rate of the field strength of the ellipsoidal bubble.

Various PIC techniques were introduced like high-order interpolation, new field solver, field ionization and boosted frame. High-order interpolation is useful for any application to reduce numerical errors. In other words, if simulations are done in a proper mesh resolution, we can lighten the number of particles drastically. Since numerical errors diverse with simulation time, the case of initially given temperature or externally given fields really needs the high-order calculation. It may be helpful studying temperature effects of some applications like Terahertz generation and Raman scattering. Boosted frame technique is useful for LWFAs since it can save simulation time dramatically. But there are arguments of using this technique because it needs field filtering and enlarged mesh size. So it has to be checked in various directions. Other groups use the boosted frame to predict the final electron energy and charges and it still well-matches with experimental results. It is also valuable to check the bubble theory using the boosted frame. This is another interesting research topic.

References

[1] T. G. Jones, K. Krushelnick, A. Ting, D. Kaganovich, C. I. Moore, and A. Morozov, "Temporally resolved Raman backscattering diagnostic of high intensity laser channeling," *Review of Scientific Instruments,* vol. 73, pp. 2259-2265, Jun 2002.

[2] H. Jang, M. S. Hur, J. M. Lee, M. H. Cho, W. Namkung, and H. Suk, "A method to measure the electron temperature and density of a laser-produced plasma by Raman scattering," *Applied Physics Letters,* vol. 93, Aug 18 2008.

[3] I. Kostyukov, A. Pukhov, and S. Kiselev, "Phenomenological theory of laser-plasma interaction in "bubble" regime," *Physics of Plasmas,* vol. 11, pp. 5256-5264, Nov 2004.

[4] H. C. Wu, B. S. Xie, S. Zhang, X. R. Hong, X. Y. Zhao, and M. P. Liu, "Bubble core field modification by residual electrons inside the bubble," *Physics of Plasmas,* vol. 17, Nov 2010.

[5] I. Kostyukov, E. Nerush, A. Pukhov, and V. Seredov, "Electron Self-Injection in Multidimensional Relativistic-Plasma Wake Fields," *Physical Review Letters,* vol. 103, Oct 23 2009.

[6] S. Kalmykov, S. A. Yi, V. Khudik, and G. Shvets, "Electron Self-Injection and Trapping into an Evolving Plasma Bubble," *Physical Review Letters,* vol. 103, Sep 25 2009.

[7] F. F. Chen, *Introduction to Plasma Physics and Controlled Fusion* vol. 1: Springer, 2006.

[8] H. Wu, "JPIC & How to make a PIC code," *arXiv,* p. 1104.3163, 2011.

[9] T. Umeda, Y. Omura, and H. Matsumoto, "Charge conservation methods for computing current densities in electromagnetic particle-in-cell simulations," *Proceedings of ISSS-7,* 2005.

[10] K. S. Yee, "Numerical Solution of Initial Boundary Value Problems Involving Maxwells Equations in Isotropic Media," *Ieee Transactions on Antennas and Propagation,* vol. Ap14, pp. 302-&, 1966.

[11] J. L. Vay, C. G. R. Geddes, E. Cormier-Michel, and D. P. Grote, "Numerical methods for instability mitigation in the modeling of laser wakefield accelerators in a Lorentz-boosted frame," *Journal of Computational Physics,* vol. 230, pp. 5908-5929, Jul 1 2011.

[12] M. Karkkainen, E. Gjonaj, T. Lau, and T. Weiland, "Low-dispersion wake field calculation tools," *Proceedings of the International Computational Accelerator Physics Conference,* 2006.

[13] J. B. Cole, "A high-accuracy realization of the Yee algorithm using non-standard finite differences," *Ieee Transactions on Microwave Theory and Techniques,* vol. 45, pp. 991-996, Jun 1997.

[14] A. Pukhov, "Three-dimensional electromagnetic relativistic particle-in-cell code VLPL (Virtual Laser Plasma Lab)," *Journal of Plasma Physics,* vol. 61, pp. 425-433, Apr 1999.

[15] Y. Sentoku, "note on Numerical Dispersion Free Maxwell Solver," *personal contact,* 2004.

[16] J. L. Vay, "Noninvariance of space- and time-scale ranges under a Lorentz transformation

and the implications for the study of relativistic interactions," *Physical Review Letters,* vol. 98, Mar 30 2007.

[17] S. F. Martins, R. A. Fonseca, L. O. Silva, W. Lu, and W. B. Mori, "Numerical simulations of laser wakefield accelerators in optimal Lorentz frames," *Computer Physics Communications,* vol. 181, pp. 869-875, May 2010.

[18] C. K. Birdsall and A. B. Langdon, *Plasma Physics via Computer Simulation (Appendix C)*: Adam Hilger, 1991.

[19] K. Y. Kim, A. J. Taylor, J. H. Glownia, and G. Rodriguez, "Coherent control of terahertz supercontinuum generation in ultrafast laser-gas interactions," *Nature Photonics,* vol. 2, pp. 605-609, Oct 2008.

[20] I. O. r. Klimo, "Simulations of Ultrashort-Pulse Laser Solid-Target Interactions," Doctor, Physical Electronics, CZECH TECHNICAL UNIVERSITY, PRAGUE, 2007.

[21] H. Hamster, A. Sullivan, S. Gordon, W. White, and R. W. Falcone, "Subpicosecond, Electromagnetic Pulses from Intense Laser-Plasma Interaction," *Physical Review Letters,* vol. 71, pp. 2725-2728, Oct 25 1993.

[22] H. Hamster, A. Sullivan, S. Gordon, and R. W. Falcone, "Short-Pulse Terahertz Radiation from High-Intensity-Laser-Produced Plasmas," *Physical Review E,* vol. 49, pp. 671-677, Jan 1994.

[23] C. C. Cheng, E. M. Wright, and J. V. Moloney, "Generation of electromagnetic pulses from plasma channels induced by femtosecond light strings," *Physical Review Letters,* vol. 87, Nov 19 2001.

[24] G. Shvets, I. Kaganovich, and E. Startsev, "Comment on "Generation of electromagnetic pulses from plasma channels induced by femtosecond light strings"," *Physical Review Letters,* vol. 89, Sep 23 2002.

[25] L. H. Cao, W. Yu, H. Xu, C. Y. Zheng, Z. J. Liu, B. Li*, et al.*, "Terahertz radiation from oscillating electrons in laser-induced wake fields," *Physical Review E,* vol. 70, Oct 2004.

[26] P. Sprangle, J. R. Penano, B. Hafizi, and C. A. Kapetanakos, "Ultrashort laser pulses and electromagnetic pulse generation in air and on dielectric surfaces," *Physical Review E,* vol. 69, Jun 2004.

[27] H. C. Wu, J. Meyer-ter-Vehn, H. Ruhl, and Z. M. Sheng, "Terahertz radiation from a laser plasma filament," *Physical Review E,* vol. 83, Mar 15 2011.

[28] Z. M. Sheng, K. Mima, J. Zhang, and H. Sanuki, "Emission of electromagnetic pulses from laser wakefields through linear mode conversion," *Physical Review Letters,* vol. 94, Mar 11 2005.

[29] H. C. Wu, Z. M. Sheng, Q. L. Dong, H. Xu, and J. Zhang, "Powerful terahertz emission from laser wakefields in inhomogeneous magnetized plasmas," *Physical Review E,* vol. 75, Jan 2007.

[30] T. Loffler, F. Jacob, and H. G. Roskos, "Generation of terahertz pulses by photoionization of electrically biased air," *Applied Physics Letters,* vol. 77, pp. 453-455, Jul 17 2000.

[31] D. J. Cook and R. M. Hochstrasser, "Intense terahertz pulses by four-wave rectification in air," *Optics Letters,* vol. 25, pp. 1210-1212, Aug 15 2000.

[32] X. Xie, J. M. Dai, and X. C. Zhang, "Coherent control of THz wave generation in ambient air," *Physical Review Letters,* vol. 96, Feb 24 2006.

[33] K. Y. Kim, J. H. Glownia, A. J. Taylor, and G. Rodriguez, "Terahertz emission from ultrafast ionizing air in symmetry-broken laser fields," *Optics Express,* vol. 15, pp. 4577-4584, Apr 16 2007.

[34] M. Clerici, M. Peccianti, B. E. Schmidt, L. Caspani, M. Shalaby, M. Giguere*, et al.*, "Wavelength Scaling of Terahertz Generation by Gas Ionization," *Physical Review Letters,* vol. 110, Jun 17 2013.

[35] N. V. Vvedenskii, A. I. Korytin, V. A. Kostin, A. A. Murzanev, A. A. Silaev, and A. N. Stepanov, "Two-Color Laser-Plasma Generation of Terahertz Radiation Using a Frequency-Tunable Half Harmonic of a Femtosecond Pulse," *Physical Review Letters,* vol. 112, Feb 7 2014.

[36] J. Yoshii, C. H. Lai, T. Katsouleas, C. Joshi, and W. B. Mori, "Radiation from Cerenkov wakes in a magnetized plasma," *Physical Review Letters,* vol. 79, pp. 4194-4197, Nov 24 1997.

[37] N. Yugami, T. Higashiguchi, H. Gao, S. Sakai, K. Takahashi, H. Ito*, et al.*, "Experimental observation of radiation from Cherenkov wakes in a magnetized plasma," *Physical Review Letters,* vol. 89, Aug 5 2002.

[38] D. Dorranian, M. Starodubtsev, H. Kawakami, H. Ito, N. Yugami, and Y. Nishida, "Radiation from high-intensity ultrashort-laser-pulse and gas-jet magnetized plasma interaction," *Physical Review E,* vol. 68, Aug 2003.

[39] H. C. Wu, Z. M. Sheng, and J. Zhang, "Powerful THz emission from laser wakefields in inhomogeneous magnetized plasmas," *Conference Digest of the 2006 Joint 31st International Conference on Infrared and Millimeter Waves and 14th International Conference on Terahertz Electronics,* pp. 142-142, 2006.

[40] A. S. Weling, B. B. Hu, N. M. Froberg, and D. H. Auston, "Generation of Tunable Narrow-Band Thz Radiation from Large-Aperture Photoconducting Antennas," *Applied Physics Letters,* vol. 64, pp. 137-139, Jan 10 1994.

[41] Y. Q. Liu, S. G. Park, and A. M. Weiner, "Enhancement of narrow-band terahertz radiation from photoconducting antennas by optical pulse shaping," *Optics Letters,* vol. 21, pp. 1762-1764, Nov 1 1996.

[42] A. Dobroiu, C. Otani, and K. Kawase, "Terahertz-wave sources and imaging applications," *Measurement Science & Technology,* vol. 17, pp. R161-R174, Nov 2006.

[43] A. Boboc, L. Zabeo, and A. Murari, "Simultaneous Cotton-Mouton and Faraday rotation angle measurements on JET," *Review of Scientific Instruments,* vol. 77, Oct 2006.

[44] G. Vieux, B. Ersfeld, J. P. Farmer, M. S. Hur, R. C. Issac, and D. A. Jaroszynski, "Plasma density measurements using chirped pulse broad-band Raman amplification," *Applied Physics Letters,* vol. 103, Sep 16 2013.

[45] G. Shvets, N. J. Fisch, A. Pukhov, and J. Meyer-ter-Vehn, "Generation of periodic

accelerating structures in plasma by colliding laser pulses," *Physical Review E,* vol. 60, pp. 2218-2223, Aug 1999.

[46] M. S. Hur, R. R. Lindberg, A. E. Charman, J. S. Wurtele, and H. Suk, "Electron kinetic effects on raman backscatter in plasmas," *Physical Review Letters,* vol. 95, Sep 9 2005.

[47] T. Miyakoshi, M. S. Jovanovic, Y. Kitagawa, R. Kodama, K. Mima, A. A. Offenberger*, et al.*, "Stimulated Raman back-scattering from a mm-scale inhomogeneous plasma irradiated with ultra-intense laser pulse," *Physics of Plasmas,* vol. 9, pp. 3552-3557, Aug 2002.

[48] N. Hafz, M. S. Hur, G. H. Kim, C. Kim, I. S. Ko, and H. Suk, "Quasimonoenergetic electron beam generation by using a pinholelike collimator in a self-modulated laser wakefield acceleration," *Physical Review E,* vol. 73, Jan 2006.

[49] A. Pukhov and J. MeyerterVehn, "Relativistic magnetic self-channeling of light in near-critical plasma: Three-dimensional particle-in-cell simulation," *Physical Review Letters,* vol. 76, pp. 3975-3978, May 20 1996.

[50] J. J. Thomson, C. E. Max, and K. Estabrook, "Magnetic-Fields Due to Resonance-Absorption of Laser Light," *Physical Review Letters,* vol. 35, pp. 663-667, 1975.

[51] C. Grebogi and C. S. Liu, "Brillouin and Raman-Scattering of an Extraordinary Mode in a Magnetized Plasma," *Physics of Fluids,* vol. 23, pp. 1330-1335, 1980.

[52] M. S. Bawa'aneh, H. M. El-Nasser, G. Assayed, S. Alyones, A. M. Alsmadi, S. Ai-Awfi*, et al.*, "Stimulated Raman scattering of extraordinary electromagnetic waves in weakly magnetized plasma," *Piers 2008 Cambridge, Proceedings,* pp. 294-300, 2008.

[53] M. N. Polyanskiy, I. V. Pogorelsky, and V. Yakimenko, "Picosecond pulse amplification in isotopic CO2 active medium," *Optics Express,* vol. 19, pp. 7717-7725, Apr 11 2011.

[54] W. L. Kruer, J. M. Dawson, and R. N. Sudan, "Trapped-Particle Instability," *Physical Review Letters,* vol. 23, pp. 838-&, 1969.

[55] ITER Physics Basis Editors, ITER Physics Expert Group Chairs, and Co-Chairs and ITER Joint Central Team and Physics Integration Unit, "Chapter 1: Overview and summary," *Nuclear Fusion,* vol. 39, p. 2137, 1999.

[56] N. A. Yampolsky, N. J. Fisch, V. M. Malkin, E. J. Valeo, R. Lindberg, J. Wurtele*, et al.*, "Demonstration of detuning and wavebreaking effects on Raman amplification efficiency in plasma," *Physics of Plasmas,* vol. 15, Nov 2008.

[57] N. A. Yampolsky and N. J. Fisch, "Limiting effects on laser compression by resonant backward Raman scattering in modern experiments," *Physics of Plasmas,* vol. 18, May 2011.

[58] T. Pisarczyk, A. A. Rupasov, G. S. Sarkisov, and A. S. Shikanov, "Faraday-rotation method for magnetic-field diagnostics in a laser plasma," *Journal of Soviet Laser Research,* vol. 11, p. 1, 1990.

[59] Y. Zhou, Z. C. Deng, Y. G. Li, C. Z. Li, J. Yi, L. C. Li*, et al.*, "Faraday rotation measurements by phase-based technique on HL-2A," *Journal of Instrumentation,* vol. 7, Jun 2012.

[60] T. Tajima and J. M. Dawson, "Laser Electron-Accelerator," *Physical Review Letters,* vol. 43, pp. 267-270, 1979.

[61] W. Lu, M. Tzoufras, C. Joshi, F. S. Tsung, W. B. Mori, J. Vieira, *et al.*, "Generating multi-GeV electron bunches using single stage laser wakefield acceleration in a 3D nonlinear regime," *Physical Review Special Topics-Accelerators and Beams,* vol. 10, Jun 2007.

[62] W. P. Leemans, B. Nagler, A. J. Gonsalves, C. Toth, K. Nakamura, C. G. R. Geddes, *et al.*, "GeV electron beams from a centimetre-scale accelerator," *Nature Physics,* vol. 2, pp. 696-699, Oct 2006.

[63] N. A. M. Hafz, T. M. Jeong, I. W. Choi, S. K. Lee, K. H. Pae, V. V. Kulagin, *et al.*, "Stable generation of GeV-class electron beams from self-guided laser-plasma channels," *Nature Photonics,* vol. 2, pp. 571-577, Sep 2008.

[64] J. Faure, C. Rechatin, A. Norlin, A. Lifschitz, Y. Glinec, and V. Malka, "Controlled injection and acceleration of electrons in plasma wakefields by colliding laser pulses," *Nature,* vol. 444, pp. 737-739, Dec 7 2006.

[65] S. P. D. Mangles, C. D. Murphy, Z. Najmudin, A. G. R. Thomas, J. L. Collier, A. E. Dangor, *et al.*, "Monoenergetic beams of relativistic electrons from intense laser-plasma interactions," *Nature,* vol. 431, pp. 535-538, Sep 30 2004.

[66] C. G. R. Geddes, C. Toth, J. van Tilborg, E. Esarey, C. B. Schroeder, D. Bruhwiler, *et al.*, "High-quality electron beams from a laser wakefield accelerator using plasma-channel guiding," *Nature,* vol. 431, pp. 538-541, Sep 30 2004.

[67] J. Faure, Y. Glinec, A. Pukhov, S. Kiselev, S. Gordienko, E. Lefebvre, *et al.*, "A laser-plasma accelerator producing monoenergetic electron beams," *Nature,* vol. 431, pp. 541-544, Sep 30 2004.

[68] A. Pukhov, S. Gordienko, S. Kiselev, and I. Kostyukov, "The bubble regime of laser-plasma acceleration: monoenergetic electrons and the scalability," *Plasma Physics and Controlled Fusion,* vol. 46, pp. B179-B186, Dec 2004.

[69] E. Esarey, R. F. Hubbard, W. P. Leemans, A. Ting, and P. Sprangle, "Electron injection into plasma wake fields by colliding laser pulses," *Physical Review Letters,* vol. 79, pp. 2682-2685, Oct 6 1997.

[70] S. Bulanov, N. Naumova, F. Pegoraro, and J. Sakai, "Particle injection into the wave acceleration phase due to nonlinear wake wave breaking," *Physical Review E,* vol. 58, pp. R5257-R5260, Nov 1998.

[71] H. Suk, N. Barov, J. B. Rosenzweig, and E. Esarey, "Plasma electron trapping and acceleration in a plasma wake field using a density transition," *Physical Review Letters,* vol. 86, pp. 1011-1014, Feb 5 2001.

[72] E. Oz, S. Deng, T. Katsouleas, P. Muggli, C. D. Barnes, I. Blumenfeld, *et al.*, "Ionization-induced electron trapping in ultrarelativistic plasma wakes," *Physical Review Letters,* vol. 98, Feb 23 2007.

[73] R. Sadighi-Bonabi and S. H. Rahmatollahpur, "A complete accounting of the monoenergetic electron parameters in an ellipsoidal bubble model," *Physics of Plasmas,* vol. 17, Mar 2010.

[74] P. Mora and T. M. Antonsen, "Electron cavitation and acceleration in the wake of an ultraintense, self-focused laser pulse," *Physical Review E,* vol. 53, pp. R2068-R2071, Mar 1996.

[75] M. S. Hur and H. Suk, "Numerical study of 1.1 GeV electron acceleration over a-few-millimeter-long plasma with a tapered density," *Physics of Plasmas,* vol. 18, Mar 2011.

감사의 말

울산과학기술대학교 박사과정으로 들어와서 정신없이 달려온 3년6개월이었습니다. 35이라는 늦은 나이에 다시 시작한 공부였지만 중요한 고비 때마다 허민섭 교수님의 지도로 지금까지 잘 연구를 수행해온 것 같습니다. 그 동안 잘 지도해주시고 좋은 결과를 낼 수 있게 성심껏 도와주신 허민섭 교수님께 감사의 말씀을 드립니다. 그리고 바쁘신 중에도 논문심사에 참여해주신 권민석 교수님, 최은미 교수님, 정모세 교수님 그리고 광주과기원의 석희용 교수님께 진심으로 감사드립니다.

연구실 생활과 연구 아이디어에 여러 도움을 준 연구실 동생들 또한 저에게는 중요한 동료들이었습니다. 저의 연구실 mate나 다름없는 김영국, 자주 볼 수 없는 신동원, 남다른 생각으로 무장한 강태연, 성실한 송형선, 언제나 긍정적인 권규빈 모두 고마운 대학원 동료들이었습니다. 또한 분위기 메이커 학부생 조재휘, 손준서에게도 고마운 마음을 전합니다. 여러 동생들 덕에 그동안 즐겁게 웃으며 지낼 수 있었고 즐거운 추억도 만들 수 있었습니다.

저의 연구주제가 이론적인 부분에 치중이 되어 있어 실전감각을 키우는데 많은 도움을 준 광주과기원의 남인혁, 김민석, 장도근, 김진주에게도 감사하다는 말을 전하고 싶습니다. 자주 만나고 여러 정보를 공유하고 도움을 주고받을 수 있었습니다.

학교생활하면서 많은 도움을 준 양현모, 류민우, 김성국, 김동성, 이인근, 최문석에게 고마움을 전합니다.

저의 연구를 마무리하고 이 논문을 내는데 많은 분들의 도움이 있었다는 것을 새삼스레 다시 깨닫게 됩니다. 마지막으로 이때껏 힘을 낼 수 있게 묵묵히 옆에서 지켜준 아내 김지애, 딸 조수아, 조수민, 어머니 권필녀 여사, 돌아가시 아버지 조복택 가족들에게 사랑한다는 말을 전합니다.

Curriculum Vitae

Name : Myung-Hoon Cho(Jo)

Birth Date : May 09, 1977

Birth Place : Daegu, Republic of Korea

Education

1996.03 ~ 2003.02	Physics, Kyungpook National University (B.S.)
2003.03 ~ 2005.02	Materials science and engineering, GIST(Gwangju Institute of Science and Technology) (M.S.)
2011.08 ~ 2015.02	Physics, UNIST(Ulsan National Institute of Science and Technology) (Ph.D)

Work Experience

2005.02 ~ 2011.09	Polarizer development for LCD Panel, LG Display

Awards

Grand prize at Korea Supercomputing Challenge, KISTI, Sep. 2013

Excellence award in Poster Presentation, KPS, Apr. 2014

Publication List

1. M.-H. Cho, Y.-K. Kim, H. Suk, B. Ersfeld, D.A. Jaroszynski and M.S. Hur, “Strong Terahertz Emission from Electromagnetic Diffusion near Cutoff in Plasma”, New J. Phys. (to be published in 2015)

2. Myung-Hoon Cho, Young-Kuk Kim and Min Sup Hur, “Measuring the magnetic field of a magnetized plasma using Raman scattering”, **Appl. Phys. Lett. 104 (2014) 141107**

3. Myung-Hoon Cho, Young-Kuk Kim and Min Sup, “Study of electron trapping by a transversely ellipsoidal bubble in the laser wake-field Acceleration”, **Phys. Plasmas 20 (2013) 093112**

4. Myung-Hoon Jo, Jung-Min Ahn, Chi-Hyuck Park and Jeong-Ki Park,
“Analysis of Light Leakage of LCD Module and Improvement by Cell Rubbing Angle”, **Mol. Cryst. Liq. Cryst. 507 (2009) 273-282**

5. Yongsam Kim, M.H. Jo, T.C. Kim, C.W. Yang, J.W. Kim, S. Hwang and D.Y. Noh, “Decomposed vicinal Coarsening Kinetics of a spinodally Si(111) surface”, **Phys. Rev. Lett. 102 (2009) 156103**

6. T.C. Kim, M.H. Jo, Y. Kim and D.Y. Noh, “Morphological evolution of ion-sputtered Pd(001) : Temperature effects”, **Phys. Rev. B 73 (2006) 125425**

7. patent(10-2014-0134834) 라만 산란을 이용한 플라즈마 진단 방법 및 장치

8. patent(10-2014-0134835) 고출력 테라헤르츠 발생 방법 및 장치

9. patent (10-2008-0095534) IPS LCD 보상필름의 좌우 색감비대칭 개선